Available online at www.sciencedirect.com
ScienceDirect
Trans. Nonferrous Met. Soc. China 32(2022) 3487−3515
Transactions of Nonferrous Metals Society of China
www.tnmsc.cn

A review of refractory high-entropy alloys

Yu-sheng TIAN, Wen-zhe ZHOU, Qing-biao TAN, Ming-xu WU,
Shen QIAO, Guo-liang ZHU, An-ping DONG, Da SHU, Bao-de SUN

Shanghai Key Lab of Advanced High-temperature Materials and Precision Forming and
State Key Laboratory of Metal Matrix Composites, School of Materials Science and Engineering,
Shanghai Jiao Tong University, Shanghai 200240, China

Received 23 September 2021; accepted 20 February 2022

Abstract: This work reviews recent progress in the alloy design, microstructure, and mechanical properties of refractory high-entropy alloys (RHEAs). What's more, the underlying strengthening mechanisms and deformation behavior are discussed. Composed mainly of near-equimolar refractory elements, RHEAs have superior mechanical properties, especially at high temperatures. However, many of them have limited room-temperature ductility. Much work has been done to solve this trade-off, and some of the RHEAs have the potential to be used for high-temperature applications in the future. In addition to their mechanical properties, RHEAs have other attractive properties, such as biocompatibility and wear resistance, which are discussed. Finally, current problems and future suggestions for RHEAs are discussed.

Key words: refractory high-entropy alloys; microstructure; high-temperature strength; mechanical properties; dislocations

1 Introduction

With rapid development of aerospace technology, there is an increasing demand for better performing high-temperature structural materials [1,2]. At present, nickel-based superalloys are used in applications where the working temperature can be as high as 1200 °C. However, owing to their melting point, nickel-based superalloys are not able to work at higher temperatures. Consequently, it is of great importance to find materials with higher melting points and better high-temperature performance.

The appearance of high-entropy alloys (HEAs) has encouraged researchers to design alloys from another perspective. HEAs were first reported by YEH et al [3] and CANTOR et al [4] in 2004. In contrast to traditional alloys which have only one or two principal elements, HEAs contain several main components in approximately equal proportions. As they are composed of multiple components, HEAs have higher configuration entropy and show very different characteristics compared with conventional alloys [5]. Most of them form a single solid-solution phase of body-centered cubic (BCC) [6−8], face-centered cubic (FCC) [9−11] or hexagonal close-packed (HCP) [12,13] structures. Moreover, HEAs have four core effects [14−16]: high entropy, lattice distortion, sluggish diffusion, and cocktail effects. The special phase formation and effects give HEAs attractive properties, such as high strength, good ductility, good corrosion resistance, and good cryogenic toughness. These findings have inspired researchers to design alloys from a new perspective.

Corresponding author: Qing-biao TAN, Tel: +86-21-54745597, E-mail: qbtan1981@sjtu.edu.cn;
Guo-liang ZHU, Tel: +86-21-54745597, E-mail: glzhu@sjtu.edu.cn

DOI: 10.1016/S1003-6326(22)66035-7

1003-6326/© 2022 The Nonferrous Metals Society of China. Published by Elsevier Ltd & Science Press

Refractory metals and alloys have very high melting points and superior high-temperature mechanical properties, making them very promising for the ultra-high-temperature applications [17]. Inspired by the idea of HEAs, researchers introduced refractory elements into HEAs, that is, refractory high-entropy alloys (RHEAs). SENKOV et al [18] conducted the first attempt to develop RHEAs, reporting MoNbTaW and MoNbTaVW in 2010. The first two RHEAs exhibited excellent properties at high temperatures, greatly exceeding superalloys in terms of melting points and high-temperature mechanical properties. However, RHEAs comprise refractory elements, inheriting their intrinsic room-temperature brittleness, which restricts their processing ability. Later, more RHEAs were developed, but most of them also exhibited limited room-temperature ductility, except for TiZrHfNbTa [19−23], one of the very few RHEAs to exhibit room-temperature tensile ductility. However, its strength at high temperatures was proven to be inadequate. Consequently, it would be of great importance to discover a combination of room-temperature ductility and high-temperature strength.

Most RHEAs form a single solid-solution phase, the solid-solution strengthening mechanism dominating the high strength and hardness at relatively low temperatures. Other methods have also been used to strengthen RHEAs, such as precipitation [24−26], grain boundary [27−29], and second-phase strengthening [30,31], making it easier for RHEAs to obtain better mechanical performance compared with conventional alloys. More recently, RHEAs with excellent mechanical properties have been designed, and the mechanisms have been established and completed by atomic simulation and calculations [32−35]. Consequently, RHEAs have great potential to become next-generation high-temperature structural materials [36−40], and publications on the subject are growing steadily, as shown in Fig. 1. However, the disadvantages of large density, poor oxidation resistance at high temperatures [41], and limited room-temperature ductility also need to be overcome for future practical applications. Accordingly, many researchers are paying more attention to alloy design and deformation mechanisms [42−45].

Research on RHEAs has become broader and deeper in recent years, and the purpose of this work is to review the recent progress in RHEAs. Based on a comprehensive understanding of reported publications, some important issues regarding RHEAs are discussed and emphasized. First, we review the concept of alloy design and preparation of RHEAs. Second, the microstructure, mechanical properties, and strengthening mechanisms are described. Based on the number of phases in RHEAs, they are divided into single-phase, dual eutectic, multi-phase, and RHEA-based composites. Other properties of RHEAs, such as biocompatibility and wear properties, are discussed. A brief summary is presented. Furthermore, the current problems associated with RHEAs are established, and several prospective viewpoints from the author’s perspective are presented.

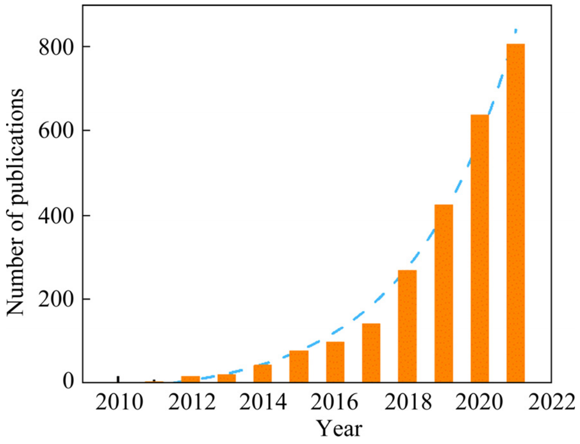

Fig. 1 Cumulative number of publications on RHEAs reported in open literature as function of year by end of August 2021

2 Methods: Alloy design and preparation

2.1 RHEA design methods

Although RHEAs represent only a fraction of HEAs, the design space is still large. Consisting of multiple principal elements, RHEAs have limited theoretical constituents. Moreover, the special effects of RHEAs (that is, high-entropy, cocktail, lattice distortion, and sluggish diffusion effects) make the empirical design methods used in conventional alloys inapplicable. Consequently, a new set of design rules for RHEAs needs to be established and design tools need to be used to simplify the design process.

2.1.1 Designing principles

The basic phase formation rules and thermodynamics of RHEAs are the same as those of HEAs. Based on the definition of RHEAs, the refractory elements are near equimolar in the alloys, each of them being a principal element. This feature makes RHEAs very different from traditional alloys in which only one element dominates. The basic parameter of RHEAs is the configuration entropy (ΔS), which can be calculated using the following equation:

$$\Delta S=-R\sum_{i=1}^{n}c_i\ln c_i \tag{1}$$

where R is the molar gas constant, which is equal to 8.314 $\mathrm{J\cdot mol^{-1}\cdot K^{-1}}$, n represents the total number of constituents, i representing the ith constituent, and c_i is the atomic concentration of the ith constituent. From the above equation, it can be seen that the configuration entropy of RHEAs is the largest when the concentration of each constituent in the system is equal. From an entropy perspective, ideal solid solutions can be divided into three types: low-entropy ($\Delta S<0.69R$), medium-entropy ($0.69R<\Delta S<1.61R$), and high-entropy alloys ($\Delta S>1.61R$). Traditional alloys are low-entropy alloys based on this definition, and are the most thermodynamically stable.

However, this parameter is not the only principal parameter. Some alloys do not meet this criterion but still show different characteristics from traditional alloys, such as the well-known MoNbTaW whose configuration entropy is $-1.39R$. Thus, it is commonly accepted that HEAs do not have to meet some definitions as long as they show unique characteristics.

One of the most obvious features of high-entropy alloys, as distinct from traditional alloys, is that they usually form a simple solid solution, BCC being the most common structure in RHEAs. However, the existing solid-solution-formation rules are primarily based on alloys with one or two principal components. From the viewpoint of atomic-size difference, chemical compatibility, and mixing entropy, ZHANG et al [46] proposed three solid-solution-formation rules to predict high-entropy alloys:

$$\delta=\sqrt{\sum_{i=1}^{n}c_i\left(1-\frac{r_i}{\bar{r}}\right)^2} \tag{2}$$

where $\bar{r}\left(=\sum_{i=1}^{n}c_ir_i\right)$ is the average atomic radius, and r_i is the atomic radius of the ith element.

$$\Delta H_{\mathrm{mix}}=\sum_{i=1,i\neq j}^{n}\Omega_{ij}c_ic_j \tag{3}$$

where Ω_{ij} $(=4\Delta H_{\mathrm{AB}}^{\mathrm{mix}})$ is regular melt-interaction parameter between the ith and jth elements, and $\Delta H_{\mathrm{AB}}^{\mathrm{mix}}$ is the mixing enthalpy of the binary liquid alloys.

$$\Delta S_{\mathrm{mix}}=-R\sum_{i=1}^{n}c_i\ln c_i \tag{4}$$

Based on an analysis of the literature, ZHANG et al [46] found that the alloys formed disordered solid solutions when $-15\ \mathrm{kJ/mol}<\Delta H_{\mathrm{mix}}<5\ \mathrm{kJ/mol}$ and $\delta<5\%$; the alloys formed ordered solid solutions when $-20\ \mathrm{kJ/mol}<\Delta H_{\mathrm{mix}}<0\ \mathrm{kJ/mol}$ and $5\%<\delta<6.6\%$.

YANG and ZHANG [47] proposed a parameter Ω to predict the solid solution formation for various multicomponent alloys as

$$\Omega=\frac{T_{\mathrm{m}}\Delta S_{\mathrm{mix}}}{|\Delta H_{\mathrm{mix}}|} \tag{5}$$

where T_{m} is the melting temperature of the alloy, which can be calculated using the mixing rule as $T_{\mathrm{m}}=\sum_{i=1}^{n}c_i(T_{\mathrm{m}})_i$ and $(T_{\mathrm{m}})_i$ is the melting temperature of the ith component. By calculating the parameters of Ω and δ for typical HEAs, it is proposed that $\Omega\geq1.1$, $\delta\leq6.6\%$ should be expected to be the criteria for forming a stabilized solid solution phase with high entropy.

In addition, GUO et al [48] proposed the valence electron concentration (VEC) criteria, which was found to be the physical parameter for controlling the phase stability of BCC or FCC solid solutions. FCC phases were found to be stable with higher VECs (≥8), and BCC phases with lower VECs (≤6.87). When the value of VEC lay between them, the alloys tended to form dual phases of FCC and BCC. The VEC of the alloys could be calculated using

$$\mathrm{VEC}=\sum_{i}^{n}c_i(\mathrm{VEC})_i \tag{6}$$

where $(\mathrm{VEC})_i$ is the VEC of the ith element. SHEIKH et al [49] summarized the VEC of typical

BCC RHEAs and concluded that RHEAs have tensile ductility only when their VEC is lower than 4.5, as shown in Fig. 2. However, the yield strength of these ductile RHEAs was always lower than that of brittle RHEAs.

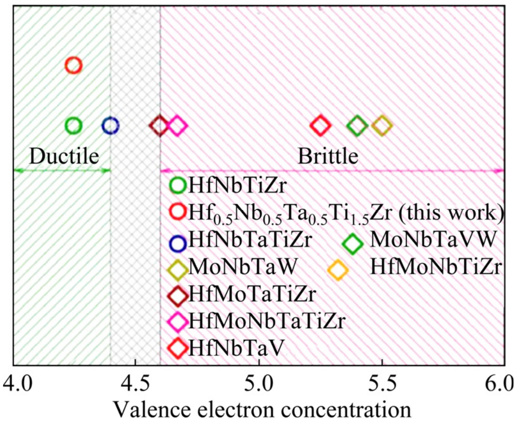

Fig. 2 Ductile and brittle BCC RHEAs divided by valence electron concentration [49] (Reproduced under the terms of the Creative Common License)

In general, the main criteria reported in the field of HEAs have been based on the Hume−Rothery criterion, among which the consideration of electron, electronegativity, and atomic-size difference has profound physical significance. However, from binary to multi-principal components, it is very difficult to find universal parameters because of the complexity of the chemical composition and the many factors affecting the formation and stability of the phase.

2.1.2 Designing methods

As stated above, although many studies have been performed on RHEAs, an enormous number of alloy systems and different compositions remain to be explored. In the early stages of RHEAs, researchers could only choose several commonly used elements to prepare and study equimolar RHEAs, and explore the effect of a certain element by adding, reducing, replacing, or changing its content. This method of alloy design is called “Polaris’s positioning” strategy and some results have been found in this way [50−53]. However, this design strategy relies on a number of experiments and is very inefficient. Subsequently, with the popularity of computer-aided simulations in materials, combinations of high-throughput computation and multiscale simulation offer great convenience for the discovery and exploration of new RHEAs. Computational methods include atomistic simulations, first-principles calculations [54], molecular dynamics (MD), Bayesian methods, and recently developed machine learning technology.

To date, the CALPHAD (calculated phase diagram) approach has been widely used with RHEAs to predict their phase formation. The quality of the results depends mainly on the database of the simulation software. ThermoCalc and Pandat are the most well-known applications for CALPHAD, and specialized databases for HEAs have been developed, such as TCHEA and PanHEA. SENKOV et al [34] calculated equilibrium phase diagrams for $Me_x(NbTiZr)_{100-x}$ alloy systems using the PanNb2018a database, where Me is Al, Cr, Fe, Hf, Mo, Re, Si, Ta, V, or W, and X ranges from 0 to 25 at.%. The authors divided the alloys into two groups. One was of a single-phase BCC region below the solidus line of all compositions and the other had a limited solution of the Me element, resulting in a new phase below the solidus line and above the solubility limit. The results were verified experimentally, and the results agreed well.

These two groups of quaternary alloy systems explored by SENKOV et al [34] are promising single-phase RHEAs and precipitation-strengthened RHEAs, respectively. SHAIKH et al [35] compared the results of 126 quaternary and 126 quinary RHEAs using CALPHAD and rule-of-mixture roles, respectively, and found that the results of the two approaches matched well. From the results, it was found that Ti, Zr, and Hf were ductilizing elements as well as reducing their densities, while Cr, Mo, and W reduced the ductility of the alloys and increased their density. In their work, a methodology was developed to rapidly screen RHEAs based on various properties.

Recently, *ab initio* methods which utilize virtual crystal approximation have become powerful tools for predicting properties of RHEAs on atomic level. MU et al [32] used the *ab initio* method to investigate the properties of RHEA systems (TiZrVMo, TiZrVMoTa, TiZrVMoTaNb, TiZrVMoTaNbCr, and TiZrVMoTaNbCrW) with increasing entropy, the experimental results matching well with the first-principle calculations. The authors found these alloys to be thermodynamically stable, the criteria in this study being satisfied by the calculated elastic constants in this structure.

MCALPINE et al [33] performed *ab initio* calculations on NbMoTaTi−X (X=W, V) to determine the vacancy change potential in both alloys. Through the calculation and experimental results, the authors found that the phase instability of NbMoTaTiW was predicted by a zero/low vacancy exchange potential and segregation in NbMoTaTiV predicted using the same elemental trends. Consequently, the vacancy exchange potential calculated using the *ab initio* method could help indicate the phase stability and elemental segregation and become a potential design tool to screen RHEAs accordingly.

2.2 Preparation of RHEAs

2.2.1 Smelting

Refractory elements can have melting points of up to ~3700 K, the difference between different refractory elements varying significantly, making it a challenge to prepare RHEAs. Thus, the method of smelting is widely used for the preparation of RHEAs. Most RHEAs are prepared by vacuum arc melting [19,50,55−59], which severely limits the size and shape of the samples. The schematic diagram is shown in Fig. 3. Moreover, because of the large differences in melting points and diffusion ability of different elements, multiple melting times are required to ensure homogeneity. In addition, since the raw materials of RHEAs are of high melting points and there exists sluggish diffusion effect in RHEAs, enough time under molten state should be ensured.

The basic concept of vacuum arc melting is to melt the raw metal materials using the high temperature produced by the arc between the crucible and electrode, after which the molten metal solidifies in the crucible. Vacuum arc melting provides the very high processing temperatures needed to melt metals, but an inert gas atmosphere is required because refractory metals have poor oxidation resistance at high temperatures. In addition, to obtain fine grains and reduce elemental segregation, a water-cooled copper crucible is commonly used to increase the solidification rate.

Induction melting is also an important method to prepare RHEAs [60,61]. The basic principle of it is similar to that of arc melting, both of which are to smelt the raw materials at high temperatures above melting points. What is different is that the high temperatures in induction melting is caused by induction while that of arc melting is caused by the arc. Besides, the size and mass of samples by induction melting have advantages over arc melting, which could prepare RHEAs of kilogram-scale instead of ~100 g of vacuum arc melting.

2.2.2 Powder metallurgy

Powder metallurgy is also a common method for preparing RHEAs [62−66]. Alloy powders are used in this way via mechanically alloying elemental mixtures or directly gas-atomizing pre-alloying ingots. The key point of this method to prepare RHEAs is to obtain alloyed powders. Pre-alloying powders by gas-atomizing work best because they are not only chemically homogeneous but also of uniform size. However, the pre-alloying powders are often of high cost and need more preparation time, making them less convenient than powders by mechanical alloying. Spark plasma sintering (SPS) and hot isostatic pressing (HIP) are utilized to consolidate powders. The schematic diagram of mechanical alloying (high energy balling)

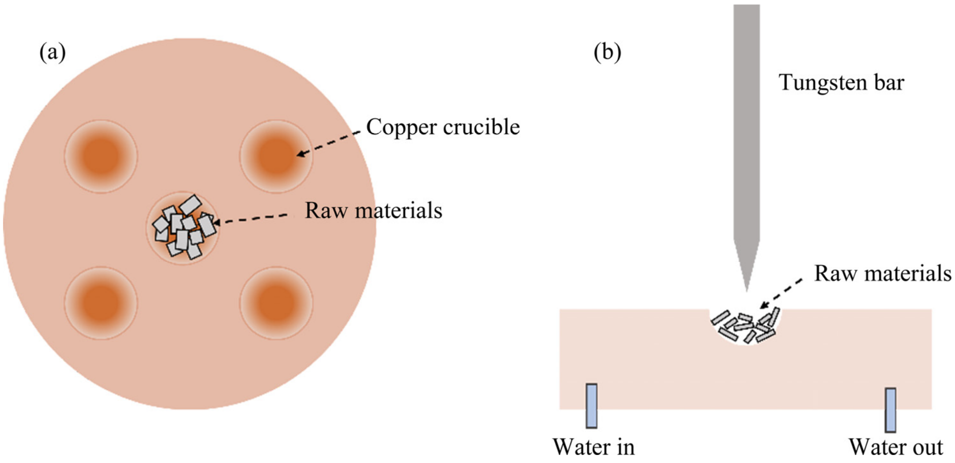

Fig. 3 Schematic diagram of vacuum arc melting: (a) Top view; (b) Front view

and SPS is shown in Fig. 4. Compared with vacuum arc melting, the samples prepared by powder metallurgy are always less dense. It is also easy to introduce impurities such as carbon and oxygen during the mechanical alloying process. However, some researchers have found it to be helpful for the mechanical properties of RHEAs as impurity elements combine with matrix elements to form strengthening phases.

ROH et al [67] prepared MoNbTaW containing metal−non-metal compounds using powder metallurgy. The β-Ta phase in the alloy attracted carbon and oxygen to form FCC metal−non-metal compounds during the sintering process, with the compounds acting as a strengthening phase at both room temperature and high temperatures. LV et al [68] introduced three types of interstitial atoms (C, N, and O) into CrMoNbWTi in order to improve the strength of the alloy. Both N and O completely reacted with the matrix elements, forming massive in situ compounds of (Nb,Ti)N and Ti_2O_3. However, C was mainly dissolved in the matrix alloy. The strengthening mechanism was attributed to the interstitial strengthening of C atoms and second phase strengthening of dispersed compounds.

2.2.3 Additive manufacturing

Additive manufacturing technologies have the advantages of high-energy input, high concentration, and high accuracy, making them suitable for high-melting-point material preparation with complex shapes. Laser cladding technology was the first additive manufacturing technology to be applied to RHEAs, having the advantage of directly forming large products. However, the products produced by laser cladding may have defects, such as poles and unmelted powders, on the surface.

Laser metal deposition is widely used in RHEAs. The use of raw powders has fewer limitations than the powder metallurgy and selective laser melting processes. In addition, the equipment is easy to obtain and can be modified from welding equipment. Many RHEAs have already been prepared using laser metal deposition. DOBBELSTEIN et al [69] were the first to prepare MoNbTaW using an equimolar mixture of elemental powders, and a single-wall structure was built. However, MoNbTaW was found to crack during the deposition process as a result of repeated heat cycles.

Later, DOBBELSTEIN et al [28,70] focused on TiZrHfNbTa and TiZrNbTa, which showed tensile ductility at room temperature. Small column specimens were successfully prepared with a BCC solid-solution phase and high hardness. The authors pointed out that laser metal deposition technology was a suitable process for screening RHEAs over a range of chemical compositions. However, the actual composition of alloys prepared by laser cladding always differed from the nominal composition, caused by large differences in the melting temperatures of different refractory

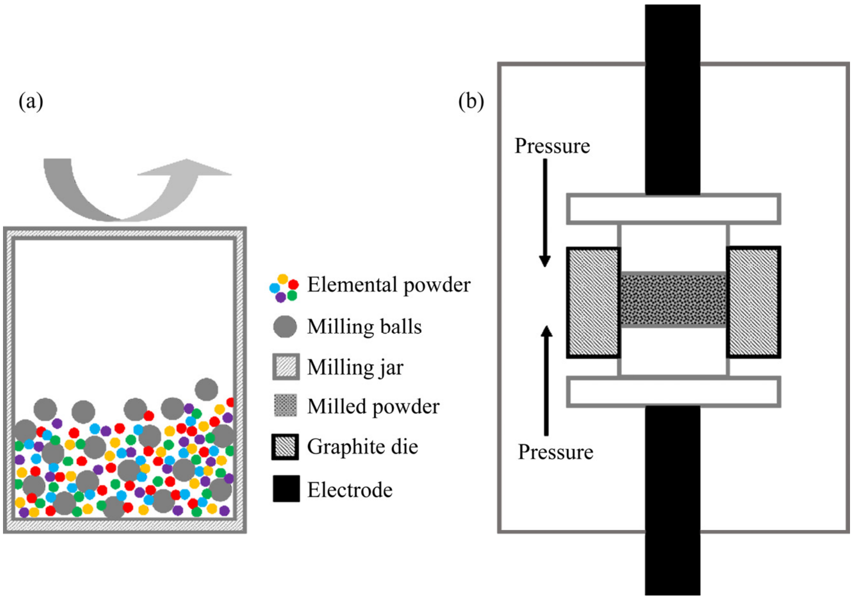

Fig. 4 Schematic diagram of mechanical alloying (high energy balling) (a) and SPS (b)

elements. More recently, another advanced additive manufacturing technology, selective laser melting technology, has attracted increasing attention. The schematic diagram of laser metal deposition and selective laser melting is shown in Fig. 5 [71]. Besides the processing parameter, the quality of the powders such as size distribution, flowability, content of water and oxygen, has a significant impact on the final product. Thus, it is of vital importance to obtain high-quality powders for selective laser melting. ZHANG et al [72] investigated the thermal-mechanical behavior of MoNbTaW prepared using selective laser melting. Their analysis demonstrated that warping and cracking resulted from uneven distribution of temperature in the entire part. Then, according to their analysis, the selective laser melting process was improved, and crack-free alloys were prepared. However, because of high melting points of RHEAs, it is very difficult to prepare pre-alloyed powders, such as superalloys and aluminum alloys, and only a few RHEAs with relatively low melting points have been prepared using this method.

3 Theory: Microstructure, mechanical properties, and strengthening mechanisms of RHEAs

Based on the number of phases, RHEAs can be divided into single-phase RHEAs, dual-phase eutectic RHEAs, other dual-phase RHEAs, multi-phase RHEAs, and RHEA-based composites with precipitates. Most reported RHEAs are of a single BCC solid-solution phase and high-entropy effect could promote the formation of solid solution. However, solid-solution strengthening weakens at high temperatures, and researchers have started to introduce new phases to strengthen the matrix. Dual-phase eutectic RHEAs have good interface bonding but relatively low melting points, based on the phase diagram. Other strengthening phases, such as precipitates, may not decrease the melting points, but it remains difficult to obtain good interfaces. Consequently, much research has been focused on non-single-phase RHEAs to achieve excellent comprehensive mechanical properties. Here, we introduce several studies on the microstructure, mechanical properties, and strengthening mechanisms based on the number of phases in RHEAs. Table 1 lists the phase structure, preparation method, and mechanical properties of some of the reported RHEAs. Figure 6 illustrates the dependence of compressive yield stress on temperature.

3.1 Single-phase RHEAs

Because of the high-entropy effect, RHEAs tend to form solid solutions of refractory elements, most RHEAs studied by researchers being in a single phase. As stated before, the first two RHEAs, MoNbTaW and MoNbTaVW, were reported in 2010 by SENKOV et al [18]. The authors designed these two RHEAs to cater for the demand for high-temperature load-bearing structures and thermal protection, successfully preparing materials with high melting points (3177 K for MoNbTaW and 2946 K for MoNbTaVW) and superior high-temperature strength (405 MPa for MoNbTaW and 477 MPa for MoNbTaVW, at 1600 °C [73]), both of which exceeded those of commonly used

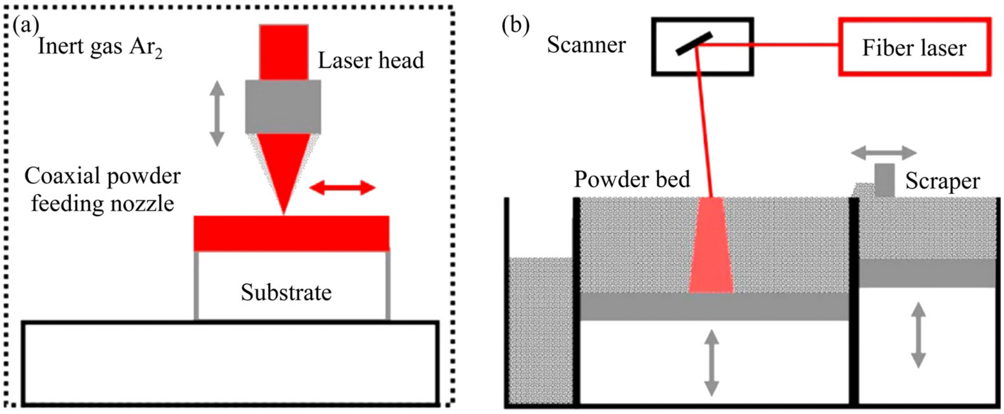

Fig. 5 Schematic diagram of laser metal deposition (a) and selective laser melting (b) [71] (Reproduced under the terms of the Creative Common License)

Table 1 Phase structure, preparation method, and mechanical properties of some reported RHEAs

Alloy	Preparation method	Phase structure	T/ °C	$\sigma_{0.2}$/ MPa	σ_U/ MPa	ε_f/ %	Ref.
MoNbTaW	VAM	BCC	23	1246	1270	1.7	[73]
			600	862	1597	13	
			800	546	1536	17	
			1000	842	1454	19	
			1200	735	943	7.5	
			1400	656	707	>40	
			1600	477	479	>40	
MoNbTaVW	VAM	BCC	23	1058	1211	2.6	[73]
			600	561		>40	
			800	552		>40	
			1000	548	1008	>40	
			1200	506	803	>40	
			1400	421	467	>40	
			1600	405	600	>40	
TiZrHfNbTa	VAM + HIP (1200 °C, 207 MPa, 1 h) + Annealing (1200 °C, 24 h)	BCC	23	929		>50	[21]
			400	790		>50	
			600	675		>50	
			800	535		>50	
			1000	295		>50	
			1200	92		>50	
	VAM	BCC+ Nanoprecipitation	23	1597		>50	[27]
			1200	356		>50	
TiZrHfNbMo	VAM	BCC	23	1719	1803	10.12	[58]
	VAM + Homogenization (1100 °C, 10 h)	BCC	23	1575	1640	9.08	[58]
			800	825	1095	>60	
			900	728	938	>60	
			1000	635	654	>60	
			1100	397	399	>60	
			1200	187	194	>60	
TiZrHfMoTa	VAM	BCC	25	1600		4	[74]
			800	1045		19	
			1000	855		>30	
			1200	404		>30	
TiZrHfNbTaMo	VAM	BCC	25	1512		12	[74]
			800	1007		23	
			1000	814		>30	
			1200	556		>30	
$AlMo_{0.5}NbTa_{0.5}TiZr$	VAM + HIP (1400 °C, 207 MPa, 2 h) + Annealing (1400 °C, 24 h)	BCC1 + BCC2	25	2000	2368	10	[23,51]
			800	1597	1810	11	
			1000	745	772	>50	
			1200	250	275	>50	
$AlNb_{1.5}Ta_{0.5}Ti_{1.5}Zr_{0.5}$	VAM + HIP (1400 °C, 207 MPa, 2 h) + Annealing (1400 °C, 24 h)	BCC	25	1280	1367	3.5	[23]
			800	728	1000	>12	
			1000	403	415	>50	
$Al_{0.4}Hf_{0.6}NbTaTiZr$	VAM + HIP (1200 °C, 207 MPa, 2 h) + Annealing (1200 °C, 24 h)	BCC	25	1841	2269	10	[23,51]
			800	796	834	>50	
			1000	298	455	>50	
			1200	89	135	>50	
$Al_{0.3}NbTa_{0.8}Ti_{1.4}V_{0.2}Zr_{1.3}$	VAM + HIP (1200 °C, 207 MPa, 2 h) + Annealing (1200 °C, 24 h)	BCC1+ BCC2	25	1965	2054	5.0	[23]
			800	362	397	>50	
			1000	236	247	>50	
$Al_{0.3}NbTaTi_{1.4}Zr_{1.3}$	VAM + HIP (1200 °C, 207 MPa, 2 h) + Annealing (1200 °C, 24 h)	BCC	25	1965	2061	5.0	[23]
			800	678	693	>50	
			1000	166	189	>50	
$Al_{0.5}NbTa_{0.8}Ti_{1.5}V_{0.2}Zr$	VAM + HIP (1200 °C, 207 MPa, 2 h) + Annealing (1200 °C, 24 h)	BCC1 + BCC2	25	2035	2105	4.5	[23]
			800	796	851	>50	
			1000	220	225	>50	
$Al_{0.4}Nb_{0.5}Ta_{0.5}TiZr_{0.8}$	VAM + Solid-solution treatment (1400 °C, 2 h)	BCC1 + BCC2 + B2	23	927		>50	[75]
$Al_{0.4}Nb_{0.5}Ta_{0.5}TiZr_{0.8}$	VAM + Solid-solution treatment (1400 °C, 2 h) + Aging (600 °C, 24 h)	BCC1 + BCC2 + B2	23	1232		10	[75]

To be continued

Continued

Alloy	Preparation method	Phase structure	T/°C	$\sigma_{0.2}$/MPa	σ_U/MPa	ε_f/%	Ref.
$Al_{0.4}Nb_{0.5}Ta_{0.5}TiZr_{0.8}$	VAM + Solid-solution treatment (1400 °C, 2 h) + Aging (700 °C, 24 h)	BCC1 + BCC2+ Zr_5Al_3	23	943		~15	[75]
$Al_{0.4}Nb_{0.5}Ta_{0.5}TiZr_{0.8}$	VAM + Solid-solution treatment (1400 °C, 2 h) + Aging (800 °C, 24 h)	BCC1 + BCC2 + Zr_5Al_3	23	934		~12	[75]
$CrMo_{0.5}NbTa_{0.5}TiZr$	VAM + HIP (1500 °C, 207 MPa, 3 h)	BCC1 + BCC2 + Laves	23	1595	2046	5.0	[19]
			800	983	1100	5.5	
			1000	546	630	>50	
			1200	170	190	>50	
CrNbTiVZr	VAM + HIP (1200 °C, 207 MPa, 2 h) + Annealing (1200 °C, 24 h)	BCC + Laves	25	1298		3	[22]
			600	1230		>10	
			800	615		>50	
			1000	259		>50	
CrNbTiZr	VAM + HIP (1200 °C, 207 MPa, 2 h) + Annealing (1200 °C, 24 h)	BCC + Laves	25	1260		6	[22]
			600	1035		>50	
			800	300		>50	
			1000	259		>50	
MoNbTaW	MA + SPS	BCC + FCC	800	1630		24	[67]
$Hf_{0.25}NbTaW_{0.5}$	VAM	BCC	23	1037	2568	42.7	[76]
			1000	584		>50	
			1200	577		>50	
			1400	455		>50	
$Hf_{0.25}NbTaW_{0.5}$	VAM + Annealing (1400 °C, 12 h)	BCC	23	942	1720	25.0	[76]
$C_{0.05}Hf_{0.25}NbTaW_{0.5}$	VAM	BCC + FCC	23	1192	2417	37.8	[76]
$C_{0.05}Hf_{0.25}NbTaW_{0.5}$	VAM + Annealing (1400 °C, 12 h)	BCC + FCC	23	1115	2044	36.7	[76]
$C_{0.1}Hf_{0.25}NbTaW_{0.5}$	VAM	BCC + FCC	23	1230	2700	41.7	[76]
$C_{0.1}Hf_{0.25}NbTaW_{0.5}$	VAM + Annealing (1400 °C, 12 h)	BCC + FCC	23	1194	2741	41.1	[76]
$C_{0.15}Hf_{0.25}NbTaW_{0.5}$	VAM	BCC + FCC	23	1265	2629	38.1	[76]
			1000	768		>50	
			1200	733		>50	
			1400	639		>50	
$C_{0.15}Hf_{0.25}NbTaW_{0.5}$	VAM + Annealing (1400 °C, 12 h)	BCC + FCC	23	1218	2646	39.7	[76]
$C_{0.2}Hf_{0.25}NbTaW_{0.5}$	VAM	BCC + FCC	23	1293	2631	36.9	[76]
$C_{0.2}Hf_{0.25}NbTaW_{0.5}$	VAM + Annealing (1400 °C, 12 h)	BCC + FCC	23	1279	2673	31.1	[76]
$C_{0.25}Hf_{0.25}NbTaW_{0.5}$	VAM	BCC + FCC	23	1317	2584	31.9	[76]
			1000	868		>50	
			1200	792		>50	
			1400	749		>50	
$C_{0.25}Hf_{0.25}NbTaW_{0.5}$	VAM + Annealing (1400 °C, 12 h)	BCC + FCC	23	1337	2799	31.0	[76]
WTaVTiCr	VAM	BCC	23	1588±128	~2200	23.4±5.7	[15]
			800	1210±43	~1700	~12	
$HfTa_{0.2}TiZr$	VAM	HCP	23	1206	1315	4.1	[45]
HfNb0.15$Ta_{0.2}$TiZr	VAM	BCC + HCP	23	406	1003	25.8	[45]
$HfNb_{0.2}Ta_{0.2}TiZr$	VAM	BCC + HCP	23	607	983	31.8	[45]
HfNb0.25$Ta_{0.2}$TiZr	VAM	BCC	23	748	843	14.2	[45]
VNbMoTa	VAM	BCC	23	1256		>25	[77]
			1000	811	~1400	>35	
ReMoTaW	VAM	BCC	23	~1100	1451	5.69	[78]
$MoNbRe_{0.5}W$	VAM	BCC	23	896±13	1232±25	7.08±0.33	[79]
$MoNbRe_{0.5}W(TaC)_{0.2}$	VAM	BCC + Eutectic	23	1071±11	1700±13	8.33±0.52	[79]
$MoNbRe_{0.5}W(TaC)_{0.4}$	VAM	BCC + Eutectic	23	1144±33	1833±34	8.81±0.26	[79]
$MoNbRe_{0.5}W(TaC)_{0.5}$	VAM	BCC + Eutectic	23	1202±15	2067±46	10.25±0.41	[79,80]
			1000	937	1551	~20	
			1200	901	1781	>35	
$MoNbRe_{0.5}W(TaC)_{0.6}$	VAM	BCC + Eutectic	23	1241±26	2351±33	9.64±0.50	[79]
$MoNbRe_{0.5}W(TaC)_{0.6}$	VAM	Eutectic	23	1340±21	2347±40	8.90±0.15	[81]
$MoNbRe_{0.5}TaW(TiC)_{0.2}$	VAM	Eutectic + Proeutectic	23	1238	1510	~7	[82]
$MoNbRe_{0.5}TaW(TiC)_{0.5}$	VAM	Eutectic + Proeutectic	23	1408	1734	~9	[82]
$MoNbRe_{0.5}TaW(TiC)_{0.8}$	VAM	Eutectic + Proeutectic	23	1438	1903	~9	[82]
$MoNbRe_{0.5}TaW(TiC)_{1.0}$	VAM	Eutectic	23	1496	1943	~9	[82]
$MoNbRe_{0.5}TaW(TiC)_{1.5}$	VAM	Eutectic + Proeutectic	23	1543	1680	6	[82]

$\sigma_{0.2}$, σ_U and ε_f are compressive yield strength, ultimate compressive strength and fracture strain, respectively

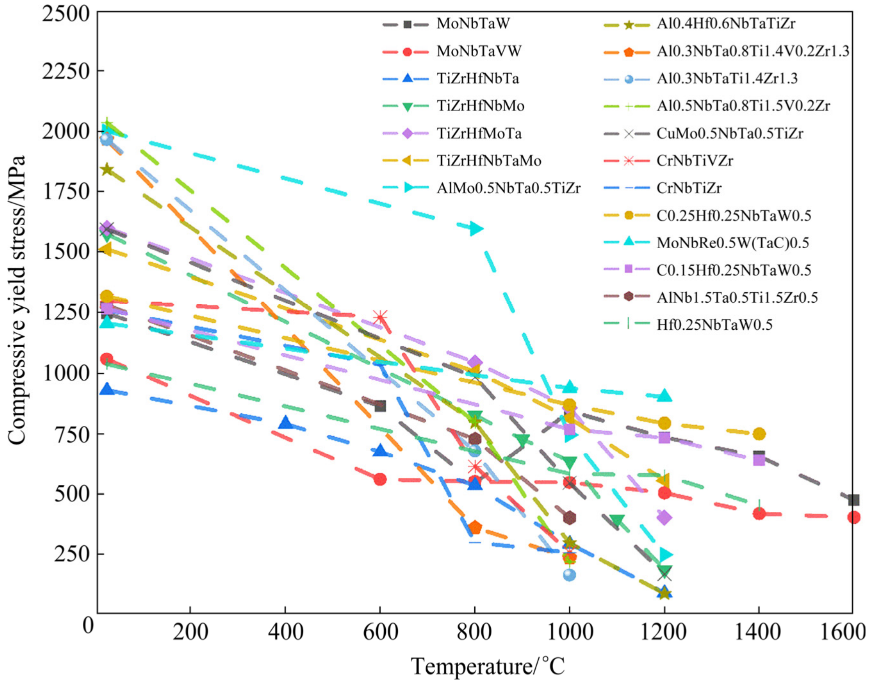

Fig. 6 Temperature dependence of compressive yield stress of part of reported RHEAs (Data are taken from Table 1)

superalloys. The yield stress of these two RHEAs dropped at temperatures below 600 °C, but was relatively insensitive to higher temperatures, suggesting that they have great potential for application in high-temperature structural materials. Both RHEAs are composed of a single phase of a BCC solid solution and show high stability at 1400 °C. Their work proved that a high-entropy design strategy could be utilized with refractory elements.

The ultra-high strength of MoNbTaW and MoNbTaVW at high temperatures is different from many elemental BCC metals and dilute BCC alloys, and traditional theories may not be useful for RHEAs. Conventional BCC metals and alloys are strong at low temperatures, but they quickly soften as the temperature increases, while the MoNbTaW and MoNbTaVW are still robust at high temperatures. As is generally known, the strengthening mechanism of BCC elemental metals and BCC alloys at low temperatures is controlled by screw dislocation movement, gliding by kink-pair nucleation, and propagation. In dilute alloys, low-temperature plasticity is understood to be controlled by kink nucleation, which can be enhanced or inhibited by solutes, while intermediate-temperature plasticity is controlled by kink glide. The intersections of kinks give rise to cross-kinks and serve as pinning points.

Breaking requires the creation of high-energy-cost point defects, creating high-energy barriers to flow. Thus, the flow stress decreases less rapidly than at low to moderate temperatures. At high temperatures, the strength of some alloys often drops abruptly. A model explaining the strengthening of BCC dilute alloys developed by SUZUKI [83] accounts for the effects of solutes on kink nucleation, kink glide, and cross-kink formation. This model has been quite successful and produced good results, but it still has several problems and limitations according to MARESCA and CURTIN [84].

MARASCA pointed out four limitations of the Suzuki model. First, there is a solute/screw interaction parameter in the Suzuki model, which assumes that the interaction energies are non-zero and equal only at the first two neighbors around the core. This assumption could not be extended to multiple solutes in the non-dilute limit, whereas the model reported by MARESCA could take the entire solute/dislocation interaction energy field in a consistent manner. Next, the Suzuki model does not consider the existence of an intrinsic energy barrier of moving segments from low-energy to high-energy positions during the kink glide as a result of spontaneous kinking. In addition, the

Suzuki model considers that the energy change during kink glide due to a particular solute configuration changes abruptly, as if the kink width is $w_k=b$. Only thereafter does SUZUKI average this result over the kink width. Although the energy scale estimated by SUZUKI is similar to MARESCA's work, the authors believe that this may lead to an overestimation of the magnitude during kink glide and to an unphysical result at $T=0$ K. Finally, the Suzuki model considers the formation of cross-kinks or dipoles to be a result of glide, without addressing the reason or quantity that might form on different gliding planes.

Based on the above advantages compared with the old model, MARESCA's theory starts from the spontaneous kinking of the screw dislocation over a characteristic length scale ζ_c (Fig. 7), determined by the solute/dislocation interactions and kink energy, and identifies three strengthening regimes: a Peierls-like mechanism, lateral kink gliding, and cross-kink unpinning. The prediction using this theory is consistent with molecular dynamics results and has also been validated experimentally, from low to high temperatures in several screw-controlled non-dilute and highly concentrated alloys. Consequently, MARESCA proposed a general theory of strengthening of screw dislocations in BCC alloys, from dilute to random ("high entropy"), extending the broadness of conventional screw dislocation strengthening.

However, the above screw dislocation theory could not explain the higher strength of MoNbTaW and MoNbTaVW (than conventional BCC alloys) at high temperatures. MARESCA and CURTIN reported an edge dislocation theory for BCC alloys [85], illuminating the origin of high strength in BCC RHEAs up to 1900 K. The authors developed the theory that the strengthening of RHEAs especially at high temperatures could be controlled by edge dislocation gliding rather than screw dislocations. This theory makes these BCC RHEAs somewhat different from elemental BCC metals and dilute BCC alloys, where screw dislocations dominate, as mentioned in SUZUKI's and MARESCA's screw dislocation theory.

Traditionally, the yield strength of BCC elemental metals is dominated by screw dislocation movement via double-kink nucleation which is activated thermally. At a low temperature of $T=0$ K, a large energy barrier exists for double-kink nucleation, leading to high strength. When the temperature is 300 K, the strength drops rapidly as the energy barrier quickly decreases. However, in some low-concentration binary alloys, the opposite is true: although the energy barrier is lower, strength increases quickly at low temperatures because of the inhibition of kink glide in the solute environment. However, low-concentration binary alloys eventually weaken at high temperatures. However, MoNbTaW and MoNbTaVW did not show

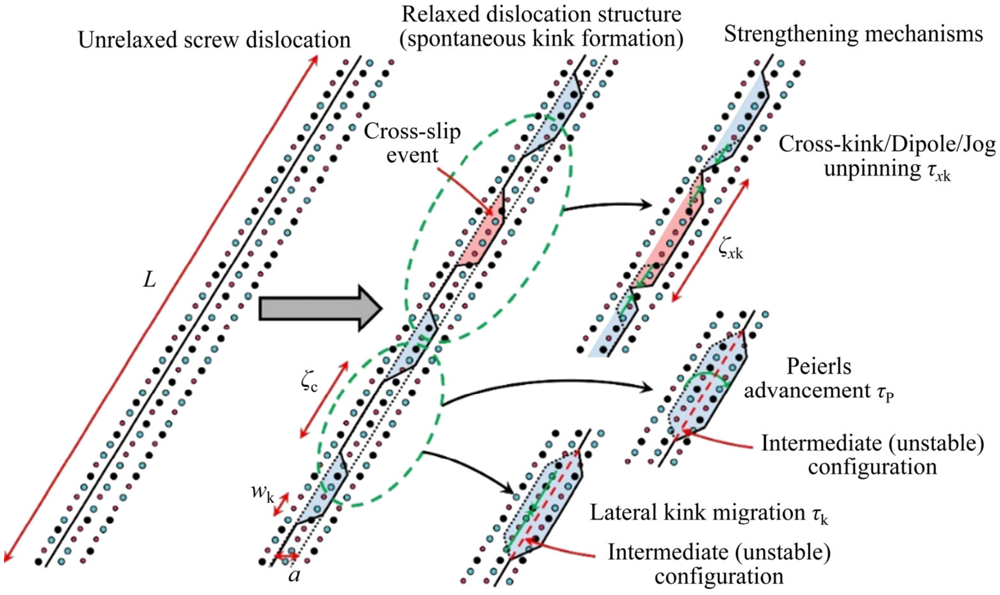

Fig. 7 Structure and motion of screw dislocation in random solute environment [84] (Reproduced under the terms of the Creative Common License)

a precipitous drop at high temperatures, even at half of their melting points. This phenomenon could not be explained by the traditional screw dislocation theory. In MARESCA's edge dislocation theory, the core argument is that the strength comes from the intrinsic complexity of the RHEAs on atomic level instead of conventional mechanisms which are easy to get weak in high-temperature diffusional/ dislocation-climb processes (Fig. 8). In this way, the dislocation must move across the random alloy itself, rather than glide or kink.

In the RHEAs, atoms are randomly arranged owing to the high-entropy effect, and thus, there is no easier way for dislocation movement, quantified by parameters ζ_c and w_c, which makes the RHEAs strong at high temperatures. As complexity is common in RHEAs, there is great potential to obtain excellent strength at high temperatures. The authors believe that the different behaviors of RHEAs at high temperatures are the result of competition for screw dislocation or edge dislocation strengthening. The above two theories by MARESCA (screw dislocation and edge dislocation) offer much help to rapidly screen and design BCC alloys with superior properties. Similar findings of edge dislocation domination in RHEAs have been experimentally observed by LEE et al [86] recently. They employed integrated in-situ neutron-diffraction, high-resolution transmission electron microscopy and recent theory and found that the high strength and strength retention of NbTaTiV and CrMoNbV are attributed to edge dislocations. Unlike in dilute alloys in previous works, their theory shows that edge dislocations in some complex HEAs can encounter very large energy barriers to glide and enable high strength at elevated temperatures. Thus, over 1000000 possible new alloys with better performance among the Al−Cr−Hf−Mo−Nb−Ta−Ti−V−W−Zr composition space were predicted guided by their theory to be explored in the future.

After MoNbTaW and MoNbTaVW, SENKOV et al reported a series of new RHEAs, such as TiZrHfNbTa [20,21], NbCrMo$_{0.5}$Ta$_{0.5}$TiZr [19,87], and AlMo$_{0.5}$NbTa$_{0.5}$TiZr [53], each of them showing unique properties compared to conventional alloys. NbCrMo$_{0.5}$Ta$_{0.5}$TiZr and AlMo$_{0.5}$NbTa$_{0.5}$TiZr had similar properties to MoNbTaW, which exhibited excellent high-temperature strength but low room-temperature ductility. In contrast to MoNbTaW and MoNbTaVW, TIZrHfNbTa showed excellent room-temperature deformation ability. At room temperature, TiZrHfNbTa could be compressed to 50% strain without any sign of fracture, being one of the very few RHEAs that could be tensile- deformed. Because of the excellent deformation ability, all studies on the deformation mechanisms of RHEAs have been conducted on the TiZrHfNbTa system.

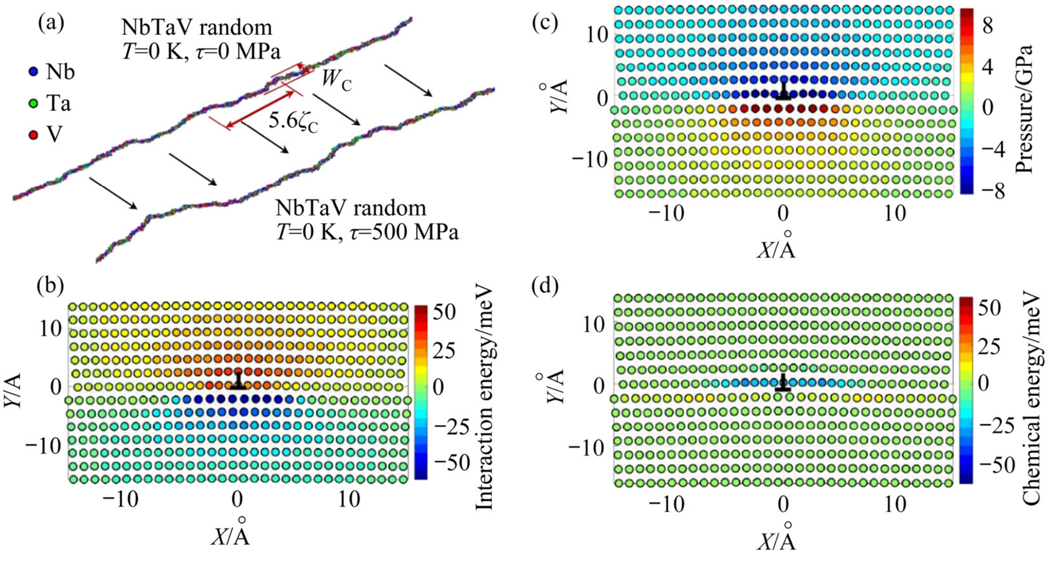

Fig. 8 Edge dislocations in model BCC NbTaV alloy: (a) Zero temperature and zero stress low-energy wavy configuration of BCC edge dislocation in true random modeled NbTaV alloy (Colors indicate atom types); (b) Solute/ edge dislocation interaction energy for a Nb solute in average-atom NbTaV alloy; (c) Pressure field of edge dislocation in average-atom NbTaV material; (d) Chemical contribution to solute/edge dislocation interaction energy in alloy [86] (Reproduced under the terms of the Creative Common License)

Room-temperature deformation of TiZrHfNbTa composed of a single solid-solution phase is controlled by a solid-solution strain- hardening mechanism, as proven by the shear bands and deformation twins observed by SENKOV et al [20]. The strain-hardening process of TiZrHfNbTa can be divided into three stages [88], as shown in Fig. 9. In Stage 1, work hardening decreases rapidly before reaching a true strain of ~3%. Subsequently, it becomes stable at ~1300 MPa during Stage 2 and then decreases when strain reaches about 10% during Stage 3. By the transmission electron microscopy (TEM) observations, in Stage 1, the plastic deformation is dominated by screw dislocation movement with the $b=a/2\langle 111\rangle$ aligned in $\langle 111\rangle$ directions, validating strong intrinsic friction stress of the alloy. The measured apparent activation volumes evolve slightly and decrease from approximately $50b^3$ to $30b^3$, the values of which are in accord with a Peierls mechanism and comparable to other BCC alloys. The TEM and X-ray diffraction (XRD) results in this work both point to a lower moving ability of screw dislocations than edge dislocations, which is typical of BCC elemental metals and alloys. Similar conclusions were drawn by LILENSTEN et al [7].

The high-temperature mechanical properties of TiZrHfNbTa are different from those of MoNbTaW and MoNbTaVW. The compressive yield strength of TiZrHfNbTa was only 92 MPa at 1200 °C, which dropped dramatically compared with that at room temperature. This behavior is consistent with conventional BCC alloys, caused by the lower mobility of screw dislocations, as mentioned before.

However, there are many interesting findings on TiZrHfNbTa, which are rarely observed in conventional BCC alloys. The most significant difference is that this alloy, after being solution-treated at 1473 K, shows a yield stress anomaly [43]. When the temperature is below 673 K, the yield stress rapidly drops as temperature increases. When the temperature reaches 873 K, further increases of temperature make the yield stress decrease once again. After investigation on its microstructures, it was found that the phase was separated into two BCC phases from 773 K to 1073 K, the HCP phase being precipitated at 773−973 K. By considering that the precipitation of the HCP phase increases the hardness, the yield stress anomaly at 873 K results from the HCP precipitation which is caused by the BCC phase separation. Thus, the TiZrHfNbTa anomaly can be attributed to phase instability.

ELETI et al [89] found a unique phenomenon in TiZrHfNbTa. The flow stress dropped sharply at the yielding point and continued to decrease as the strain increased. Their work was conducted between 1000 and 1200 °C, where the phase was stable. With interrupted compression tests, it was found that the precipitous drop of the stress might have been caused by dislocation unlocking, which might be caused by solute atom(s) atmosphere or short-range ordering. The dynamic recrystallization behavior was also thought to cause flow softening of the alloy.

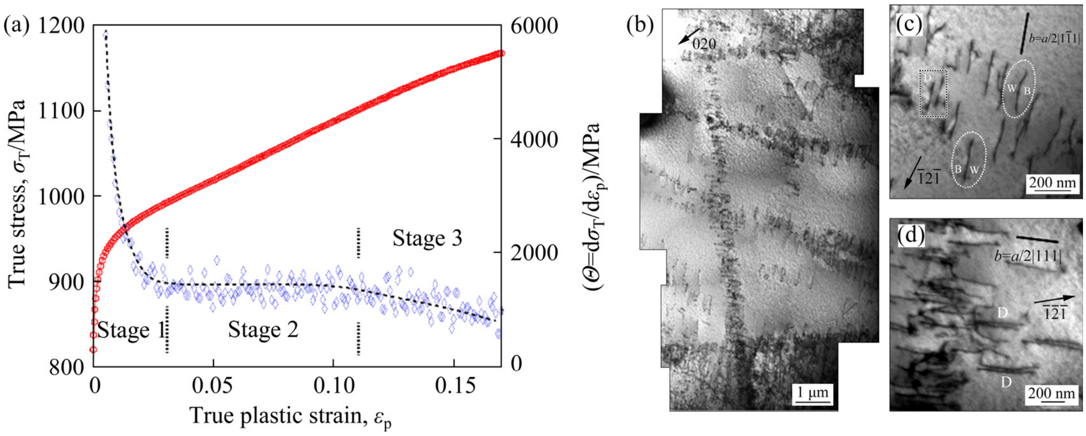

Fig. 9 Evolution of true stress and work hardening with plastic strain (a); TEM bright-field micrograph of dislocation patterning for ε_P=0.85% (b); $b=a/2\langle 111\rangle$ defects in bands (c, d) [88] (Reproduced under the terms of the Creative Common License)

CHEN et al [90] observed flow serration in TiZrHfNbTa, which was attributed to dynamic strain aging and is often observed in FCC RHEAs. They studied this behavior at 573−823 K to understand the interactions between solutes and dislocations in RHEAs. This flow-serration behavior was observed under all conditions, and besides the strength and curve shape, the temperature along with the strain rate also made changes to the flow-serration type and onset of the serrated flow (Figs. 10 and 11). The authors provide a theoretical model that can accurately predict the behavior of the onset of serrated flow at varying temperatures. The model can be used to define the process window when the application of RHEAs comes into practice. All of these above-mentioned studies can help guide future practical applications of alloys at different temperatures.

TiZrHfNbTa is not the only RHEA that exhibits tensile ductility. Some of the derived RHEAs from TiZrHfNbTa, such as HfNbTaZr and $HfNb_{0.18}Ta_{0.18}Ti_{1.27}Zr$, show tensile and compressive ductility of more than 50%. However, the low yield strength (YS) of these TiZrHfNbTa-series RHEAs, especially at high temperatures, may limit their application. LEI et al [91] proposed a method to introduce 2 at.% oxygen into TiZrHfNb, simultaneously enhancing the strength and ductility of the alloy, and realizing the long-time pursuit. The oxygen introduced into the RHEAs formed ordered oxygen complexes, which are different from conventional oxide particles or frequently occupying random interstitials. Such complexes are atomic complexes enriched with O, Ti, and Zr, which were promoted by the formation of chemical short-range ordering among some of the substitutional elements in the matrix. The dislocation shear mode of the matrix alloy is planar slip, while with the occurrence of the ordered oxygen complexes, it turns to wavy slip, which further facilitates double cross-slip and multiplication of dislocations by the formation of

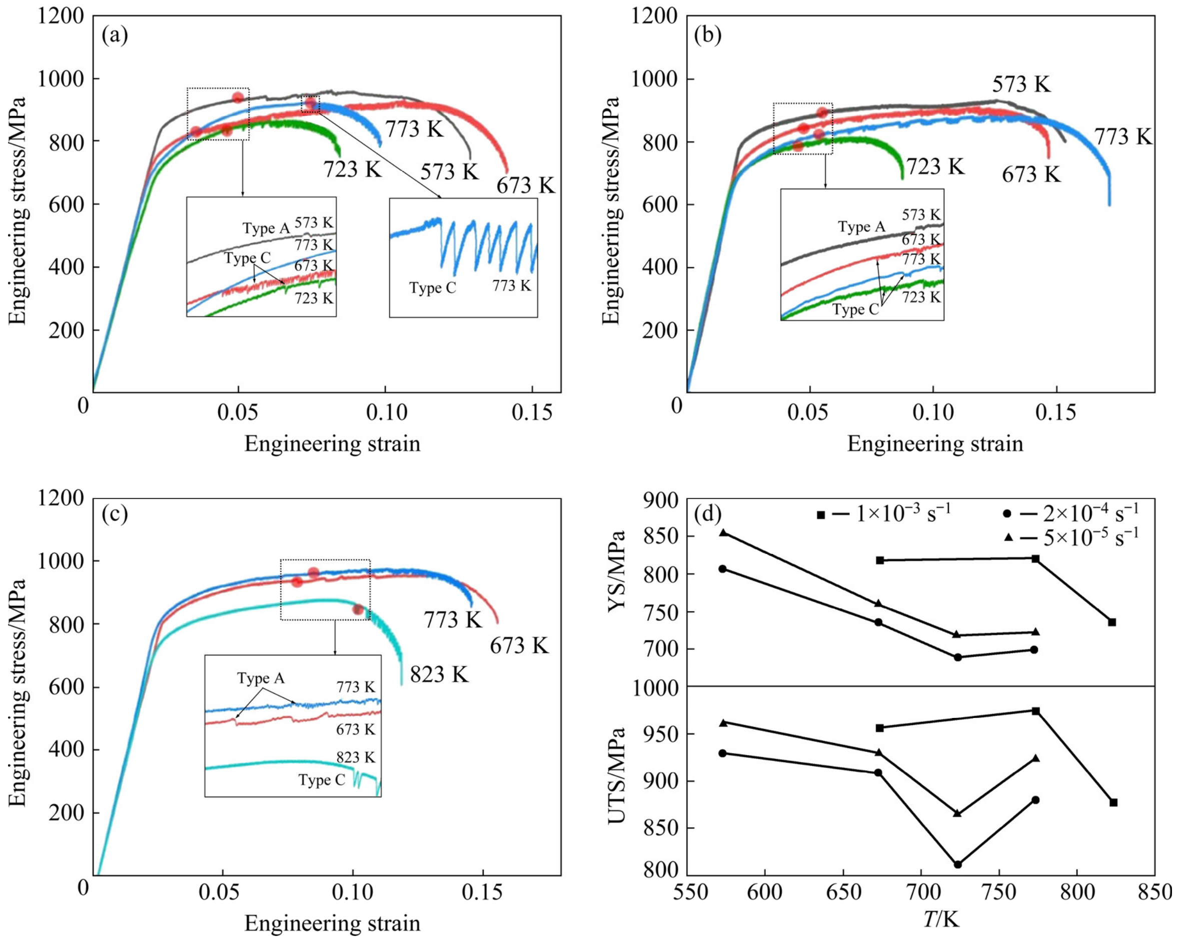

Fig. 10 Temperature dependence of uniaxial tensile behavior of TiZrHfNbTa alloy at strain rates of 5×10^{-5} s^{-1} (a), 2×10^{-4} s^{-1} (b) and 1×10^{-3} s^{-1} (c); Temperature dependence of yield strength (YS) and ultimate tensile strength (UTS) at three applied strain rates (d) [90] (Reproduced under the terms of the Creative Common License)

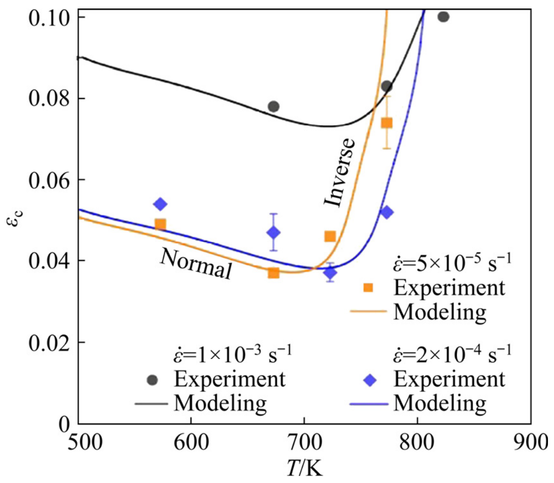

Fig. 11 Variation of critical serration strain with temperatures and strain rates predicted from model by CHEN et al alongside experimental data (symbols) [90] (Reproduced under the terms of the Creative Common License)

Frank–Read sources. They concluded that in alloys where interstitial elements could cause embrittlement this strain-hardening mechanism related with ordered oxygen complexes played an important role, especially those containing Ti, Zr, or Hf elements in which tuning the stacking fault energy and exploiting athermal transformations make little effort to improve mechanical properties. Their results raise great concern about the vital role of interstitial solid solution strengthening and related ordering strengthening mechanisms in RHEAs.

The basic strengthening mechanism of RHEAs is a solid-solution strengthening mechanism due to its random and complex composition. The first solid-solution strengthening mechanism for RHEA was proposed by SENKOV et al [20] to explain its high stress and hardness compared to the role of mixture values. Traditional solid-solution strengthening mechanisms were developed for conventional alloys, where the content of the solvent could exceed 60%−70%. In RHEAs, all composition elements are both solutes and solvents that interact with each other. Thus, the traditional solid-solution strengthening mechanisms do not apply here. Consequently, they attempted to take the difference of atomic size and shear modulus of each element into consideration. In contrast to traditional theories, they estimated the local environment around each element under the assumption that the local atomic concentration is the same as the average concentration of the alloy. The estimated values of dislocation force are approximately an order of magnitude larger than those reported for binary solid solutions. The YS predicted using this model agrees well with the experimental value. Based on this solid-solution strengthening mechanism, several modified theories were subsequently reported and successfully used to explain the strengthening of the corresponding RHEAs [29,92−94].

3.2 Dual-phase eutectic RHEAs

Limited by the solid-solution strengthening mechanism, most single-phase RHEAs are not as strong as MoNbTaW, especially at high temperatures. However, introducing second phases is a very efficient way to improve their mechanical properties. The second phases commonly observed in RHEAs include eutectic phases, precipitates, and other reinforcements. To meet the need for high-power armor piercing projectiles and other gradient materials, WEI et al [78] replaced Nb with Re in MoNbTaW as Re has a high density and could improve the ductility of some BCC elements.

The MoReTaW was composed of three disordered solid-solution phases, which was mainly caused by large differences in melting point of the elements. The substitution of Nb with Re successfully enhanced the compressive strength to 1451 MPa and the failure strain to 5.69%, respectively, ~20% and ~170% higher than those of MoNbTaW. The smaller atomic size of Re contributed most to the significant improvement of mechanical properties of the alloy, which was explained by the solid-solution strengthening mechanism, as stated earlier. Besides, the precipitation strengthening mechanism also worked here as β-Ta-rich particles dispersed uniformly in the matrix.

Since Re was proven to be useful in improving the mechanical properties of MoNbTaW, WEI et al [95] performed a series of experiments to study its effect along with the introduction of carbides. They successfully prepared MoNbRe$_{0.5}$W(TaC)$_x$ matrix composites using vacuum arc melting. The TaC-containing composites consisted of a BCC solid-solution phase and multicomponent carbide solution. The MC-type carbide phase and BCC phase formed a laminar eutectic microstructure distributing along the grain boundaries. The addition of TaC significantly improved the mechanical properties of the RHEA.

The $\text{MoNbRe0.5W(TaC)}_{0.6}$ matrix composites exhibited high microhardness, YS, and compressive strength of HV 615, 1241 MPa, and 2351 MPa, respectively, as a result of the precipitation strengthening and fine-grained strengthening. The mobility of dislocations and phase interface was effectively inhibited by MC carbide phase. At the same time, the formation of fine carbides could refine the grains of BCC phase and provide more interfaces, which improved the strength by fine-grained strengthening mechanism.

The fracture ductility first increased and then decreased, the composite reaching a maximum value of 10.25% when x=0.5. WEI et al [80] found the fine-grained strengthening caused by TaC introduction to be the main reason for the increase of ductility. With finer grains of the matrix, plastic deformation could distribute in more grains, which reduced the stress concentration. Besides, the high volume fraction of the relatively ductile BCC phase also contributed to the good ductility of the composites. However, further increase in TaC addition caused the volume fraction decrease of BCC phase, resulting in stronger but less ductile composites. Thus, a appropriate addition of TaC could simultaneously enhance the strength as well as the ductility of the composite.

$\text{MoNbRe}_{0.5}\text{W(TaC)}_{0.5}$ and $\text{MoNbRe}_{0.5}\text{W(TaC)}_{0.6}$ composites exhibited excellent comprehensive mechanical properties that were better than most of the reported RHEAs. Indeed, not only the room-temperature mechanical properties but also high-temperature properties could be enhanced in this way.

WEI et al [80] systematically investigated the microstructures and mechanical properties of $\text{MoNbRe}_{0.5}\text{W(TaC)}_{0.5}$ composites. The phases and laminar eutectic microstructure remained stable even after annealing at 1300 °C for 168 h, indicating high phase stability as well as structural stability. The composite showed high compressive yield strength at high temperatures (937 MPa at 1000 °C and 901 MPa at 1200 °C), which was much higher than that of the reported RHEAs and their composites. The semi-coherent interface between the carbide and matrix phases and the orientation relationship of $[111]_{\text{BCC}}//[011]_{\text{FCC-MC}}$, $(101)_{\text{BCC}}//(200)_{\text{FCC-MC}}$ did the major contribution to the balanced mechanical properties of the composites, which had high strength and high ductility at the same time (Fig. 12).

The strengthening mechanisms of this RHEA composite can be explained as follows: First, by calculating the mismatch parameter and TEM observations, the BCC matrix phase is semi-coherent with the FCC-MC carbide phase. In the deformation process, the semi-coherent interfaces pin the dislocations and improve the work hardening of the composites. Second, the interaction of cross-slip and pinning of the composites inhibits dislocation slipping, thereby increasing work hardening. Moreover, interactions among coplanar dislocations, stacking faults, and

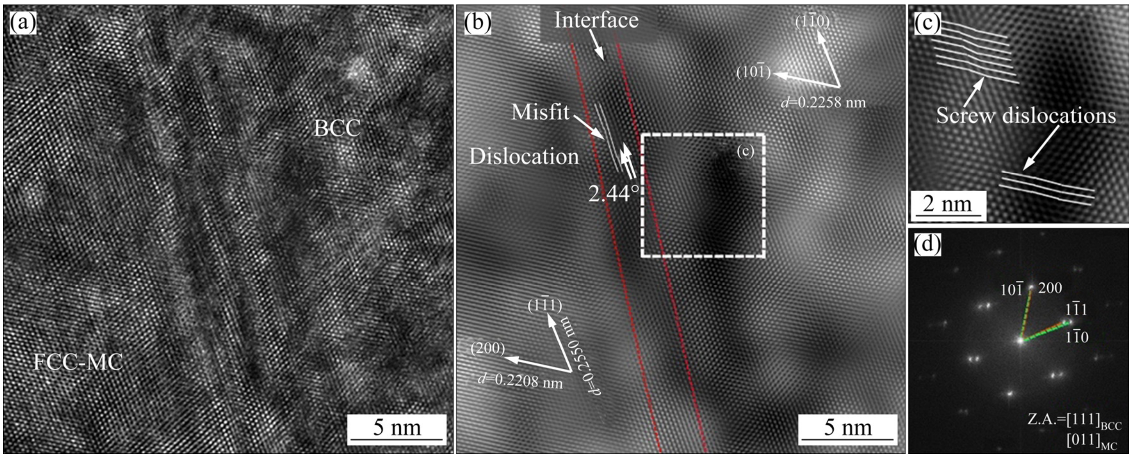

Fig. 12 TEM micrographs of phase interface after compression at 1200 °C: (a) HRTEM image; (b) Fourier-filtered image of phase interface; (c) Enlarged image of white outlined region in (b) showing screw dislocations in BCC structure near interface; (d) FFT patterns of image (a) showing relationship between BCC HEA and FCC-MC carbide [80] (Reproduced under the terms of the Creative Common License)

twins in the carbides are suppressed during the deformation process, resulting in dislocation accumulation, which requires more stress for further deformation.

Consequently, the authors conclude that the high compressive strength of MoNbRe$_{0.5}$W(TaC)$_{0.5}$ composite is contributed by the phase interface, dislocation entanglement, and twin boundaries together. Their finding is an important contribution to future high-temperature structural materials. Besides TaC, TiC is also widely used in metal matrix composites (MMCs) because it can form eutectic microstructures and carbides with many refractory elements. In this study, WEI et al [82] designed MoNbRe$_{0.5}$TaW(TiC)$_{0.5}$ matrix composites with a eutectic microstructure similar to that of MoNbRe$_{0.5}$W(TaC)$_x$ (Fig. 13) and the MoNbRe$_{0.5}$TaW(TiC)$_{1.0}$ with fully eutectic microstructures reached a maximum compressive strength of (1943±13) MPa, which is even higher than that of the MoNbRe0.5W(TaC)$_{0.6}$ composite. Thus, the eutectic strategy was verified to be useful for RHEAs.

3.3 Other RHEAs and RHEA-based composites

RHEAs always show a drop in strength with increasing temperature as solid-solution strengthening weakens at high temperatures. Thus, to improve their high-temperature mechanical properties, other strengthening mechanisms are required, and some dual- or multi-phase RHEAs (RHEA-based composites) have been developed.

Generally speaking, intermetallic compounds are considered as strengthening phases. Most of the Al-containing RHEAs have a BCC+B2 two-phase microstructure like $\gamma+\gamma'$ microstructure in nickel-based superalloys and many of them own high strength at high temperatures. However, they are brittle at room temperature. SENKOV et al [23] added Al to several RHEAs to reduce density, increase high-temperature strength and specific strength, and improve oxidation resistance. In their study, three of the six alloys, AlMo$_{0.5}$NbTa$_{0.5}$TiZr, Al$_{0.3}$NbTaTi$_{1.4}$Zr$_{1.3}$ and Al$_{0.5}$NbTa$_{0.8}$Ti$_{1.5}$V$_{0.2}$Zr, contain two bcc phases with very similar lattice parameters. The two BCC phases are present in the form of interpenetrating nano-lamellar creating basket weave nanostructure inside grains. Further investigation by SENKOV et al [95] on the AlMo$_{0.5}$NbTa$_{0.5}$TiZr alloy shows that this alloy was composed of a nano-scale mixture of two phases produced by the decomposition from a high-temperature BCC phase. The first phase is present in the form of cuboidal-shaped nano-precipitates with a disordered BCC structure while the second phase is present in the form of channels between the cuboidal nano-precipitates with an ordered B2 structure, as shown in Fig. 14. These two phases are

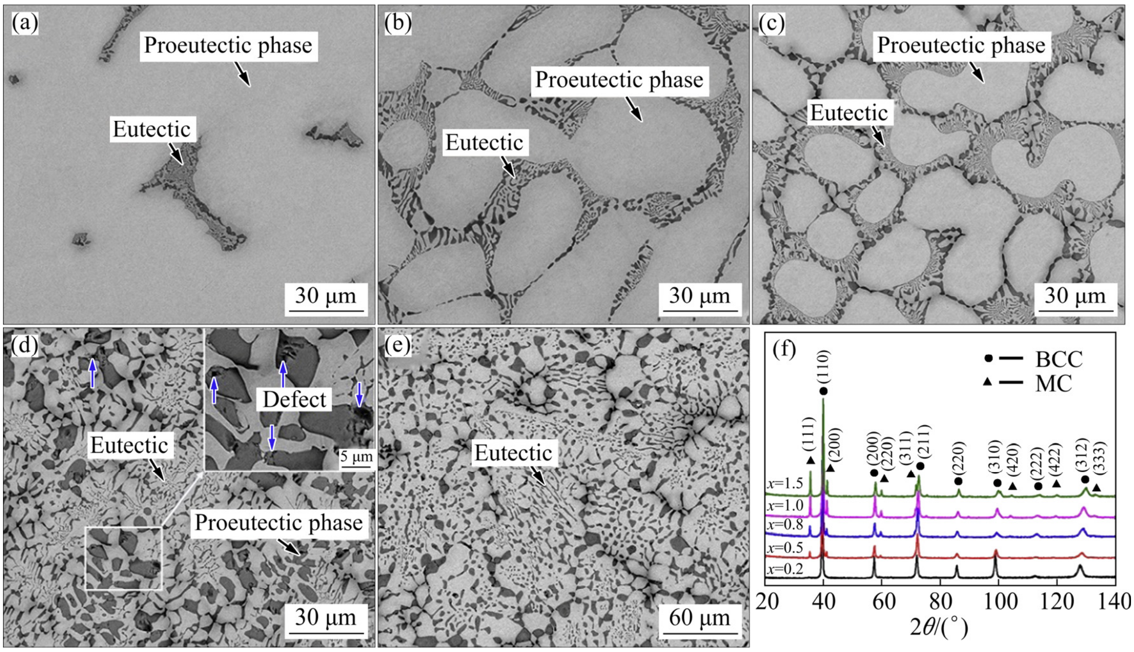

Fig. 13 SEM images (a−e) and XRD patterns (f) of MoNbRe0.5TaW(TiC)$_x$ composites: (a) x=0.2; (b) x=0.5; (c) x=0.8; (d) x=1.5; (e) x=1.0 [82] (Reproduced under the terms of the Creative Common License)

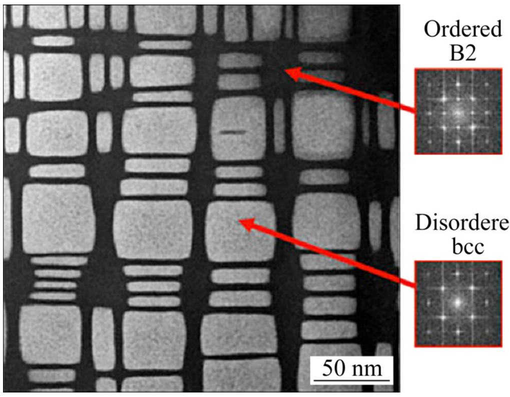

Fig. 14 Scanning transmission electron microscopy (STEM) high-angle annular dark-field image and fast Fourier transforms (inside red squares) recorded from survey sample extracted from inside-grain region (reprinted by permission of Taylor & Francis Ltd.) [95,98]

coherent with each other and the microstructure is explained by nucleation-and-growth and spinodal decomposition mechanisms. Owing to the BCC+B2 microstructure, $AlMo_{0.5}NbTa_{0.5}TiZr$ alloy shows exceptional high yield strengths superior to nickel-based superalloys from 20 to 1200 °C.

Precipitation strengthening has proven to be useful at high temperatures. YANG et al [27] observed precipitation in as-cast TiZrHfNbTa, the compressive YS at 1200 °C being significantly better (improving from 92 to 356 MPa), about three times higher than the reported data. This significant improvement could be attributed to precipitation strengthening by nanoparticles. GUO et al [96,97] designed $(Mo_{0.5}NbHf_{0.5}ZrTi)_{BCC}/M_5Si_3$ in situ composites by adding Si to $Mo_{0.5}NbHf_{0.5}ZrTi$. The addition of Si promotes the formation of an intermetallic M_5Si_3 phase with an HCP structure and an increase in hardness and strength. As the addition of Si increases, the microstructure of the composites changes from hypoeutectic to eutectic and finally to hypereutectic (Fig. 15). The fracture strain of Si0.1 is improved owing to the fine-grained mechanism and weaker solution strengthening mechanism of the matrix phase. With more Si addition, the fracture strain decreases as a result of more M_5Si_3 phases in the matrix and larger size of them.

Because many refractory elements are strong carbide-forming or nitride-forming elements, the introduction of carbon or nitrogen into RHEAs always leads to multiple strengthening mechanisms working together, such as the second-phase strengthening, precipitation mechanism (particle shearing and Orowan bypass mechanisms), load-bearing effect, and dislocation strengthening.

The second-phase strengthening (composite models) is widely applied in composite materials. The strength of the composites (σ_{com}) composed of the matrix phase and precipitation using this model can be calculated as follows:

$$\sigma_{com}=\sigma_m \cdot V_m+\sigma_p \cdot V_p \tag{7}$$

where σ_p and σ_m are the yield strengths of the precipitates and the matrix, and V_p and V_m are the volume fractions of the precipitates and the matrix ($V_m=1-V_p$), respectively (which could be measured by ImageJ software using SEM or TEM images). However, this model is very rough and does not consider other micro-interactions.

Precipitation strengthening is common in metal-matrix composites. When the size of the precipitates is large or the interface between the matrix and precipitates is incoherent, the dislocations bypass the precipitates. When the precipitates are sufficiently fine or have a coherent interface with the matrix, a particle shearing mechanism occurs.

In calculating the contribution of the dislocation shearing mechanism, three mechanisms are taken into account: coherency strengthening ($\Delta\sigma_{CS}$) mechanism, modulus strengthening ($\Delta\sigma_{MS}$) mechanism, and order strengthening ($\Delta\sigma_{OS}$) mechanism [99]. $\Delta\sigma_{CS}$ originates from the elastic interaction between the strain fields which are caused by coherent precipitates and dislocations. $\Delta\sigma_{MS}$ comes from the shear modulus difference of the matrix and precipitates. $\Delta\sigma_{OS}$ takes place with dislocations which shear ordered precipitates, leaving antiphase boundary (APB) on the slip plane of the precipitates. The calculation of three strengthening mechanisms of dislocation shearing mechanism is as follows:

$$\Delta\sigma_{CS}=M\alpha(G\varepsilon_c)^{3/2}\left(\frac{rf}{0.5Gb}\right)^{1/2} \tag{8}$$

$$\Delta\sigma_{MS}=M\times 0.0055\times(\Delta G)^{3/2}\left(\frac{2f}{G}\right)^{1/2}\left(\frac{r}{b}\right)^{\frac{3m}{2}-1} \tag{9}$$

$$\Delta\sigma_{OS}=M\times 0.81\times\frac{\gamma_{apb}}{2b}\times\left(\frac{3\pi f}{8}\right)^{1/2} \tag{10}$$

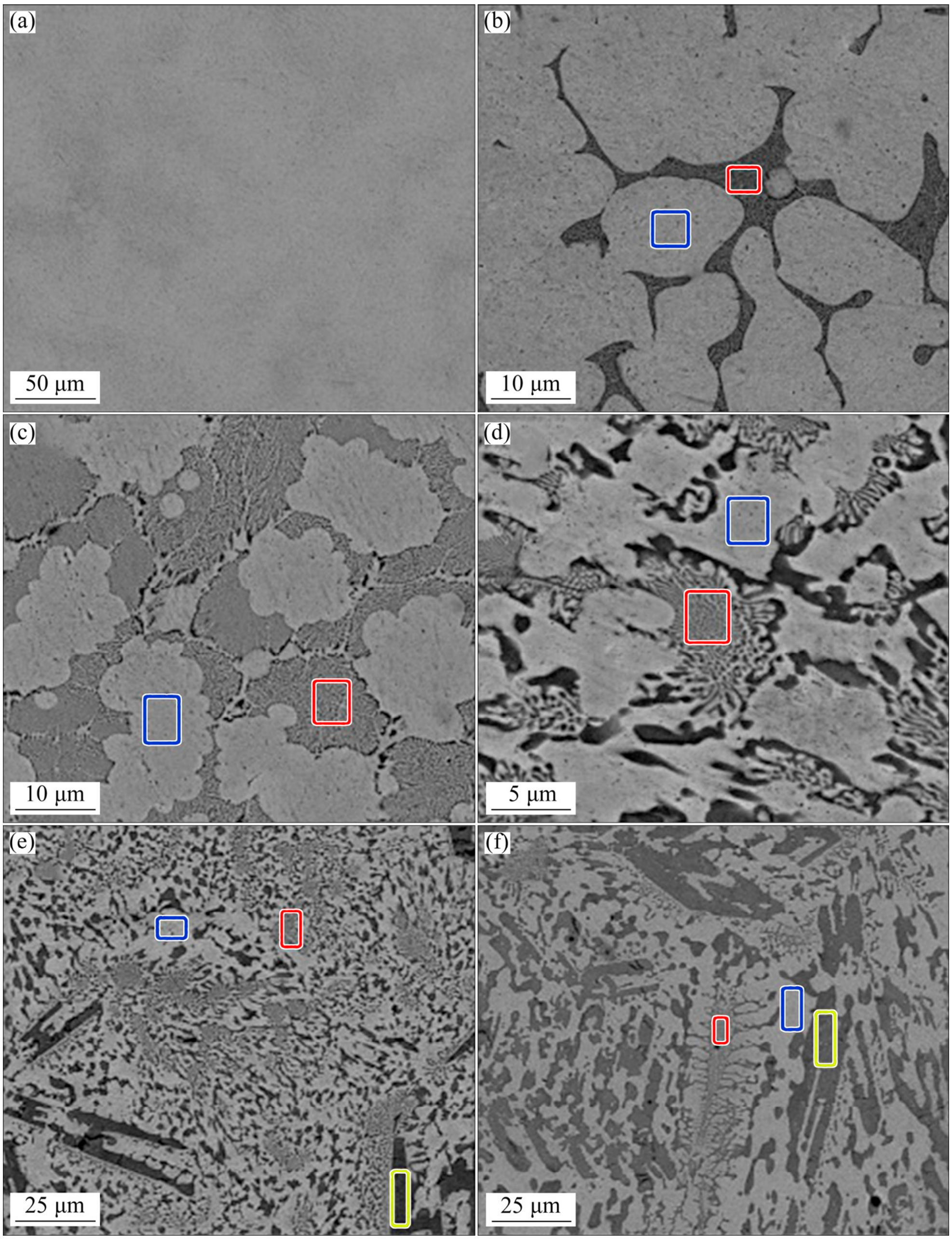

Fig. 15 SEM-BES images of as-cast Mo0.5NbHf0.5ZrTiSi$_x$ alloy: (a) x=0; (b) x=0.1; (c) x=0.3; (d) x=0.5; (e) x=0.7; (f) x=0.9 [97] (Reproduced under the terms of the Creative Common License)

where M is the Taylor factor of matrix; α is a constant; G is the shear modulus of matrix; ε_c is the constrained lattice misfit, and ε_c=2/3ε; r and f are the average particle diameter and the volume fraction of precipitates; b is the magnitude of Burgers vector; ΔG is the shear modulus difference between the precipitates and the matrix; m is a constant here for edge dislocations; γ_{apd} is the APB energy of the precipitates.

The strength improvement caused by the dislocation bypass mechanism can be expressed as follows [100]:

$$\Delta\sigma_{\text{Oro}}=\frac{MGb}{2.36\pi}\cdot\frac{1}{\lambda-r}\cdot\ln\left(\frac{r}{2b}\right) \tag{11}$$

where λ is the spacing between the neighboring reinforcements. The value of λ can be calculated using Eq. (12) under the condition where precipitation is uniformly dispersed in the matrix:

$$\lambda=r\cdot\sqrt[3]{\frac{\pi}{6f}} \tag{12}$$

The shear lag model is often used in composites containing fiber-shaped reinforcements.

It is the basic concept of load transfer theory in which the stress is transferred from the matrix to the reinforcements by means of interfacial shear stress. In this model, the interface between the matrix and the reinforcements is thought to be well bonded. The strength improvement due to the load transfer effect can be calculated using Eq. (13) [101], as follows:

$$\Delta\sigma_{\mathrm{LT}}=\sigma_{\mathrm{m}}\left[\frac{V_{\mathrm{p}}(S+2)}{2}+f\right] \tag{13}$$

where $\Delta\sigma_{\mathrm{LT}}$ is the yield strength increment caused by load transfer effect, and σ_{m} is the yield strength of the matrix alloy. S is the average aspect ratio (length to diameter) of the precipitates.

For refractory high-entropy alloy matrix composites, the cooling process from the processing temperature to room temperature results in local stress in the vicinity of the precipitates owing to the large difference in the coefficient of thermal expansion (CTE) between the matrix and the reinforcements. The localized stress increases the dislocation density in the matrix, which strengthens the composites. The strength increment ($\Delta\sigma_{\mathrm{Dis}}$) caused by the thermal expansion dislocation strengthening can be expressed by Eq. (14) [102], as follows:

$$\Delta\sigma_{\mathrm{Dis}}=M\alpha Gb\sqrt{\rho} \tag{14}$$

where M, α, G and b are the Taylor factor, dislocation hardening parameter, shear modulus, and magnitude of Burger's vector for the RHEA matrix, respectively, and ρ is the increased dislocation density caused by thermal expansion mismatch, which can be calculated as follows [103]:

$$\rho=\frac{12V_{\mathrm{p}}\Delta T\Delta C}{b\left(1-V_{\mathrm{p}}\right)d} \tag{15}$$

where ΔT is the temperature difference between the vacuum arc melting process and room temperature. ΔC is the difference in CTE between the matrix and precipitation; d is the average size of the reinforcements measured by ImageJ software using SEM or TEM images.

The basic strengthening mechanisms are stated above, and, in most RHEAs, multiple mechanisms often work together to enhance the mechanical properties. LV et al [68] prepared CrMoNbWTi co-doped with C, N, and O atoms using mechanical alloying and SPS. C atoms were primarily dissolved in the matrix while N and O atoms reacted with the matrix elements forming massive (Nb,Ti)N and Ti_2O_3 precipitates in the matrix. The RHEA with co-doped nonmetallic atoms exhibited a strength up to 4345 MPa and hardness of 11.88 GPa. The solid-solution strengthening, grain boundary strengthening, Orowan strengthening, C atom interstitial strengthening, and intergranular compounds of (Nb,Ti)N and Ti_2O_3 contributed together to the extremely high properties of this composite.

For most multi-phase RHEAs, there exists a trade-off of strength and ductility, though the strength both at room temperature and high temperatures are very attractive. Poor room-temperature ductility severely restricts its future industrial application. Therefore, to realize a good combination of ductility and strength is of more importance and thus an appropriate choice of the strengthening phase is crucial. WU et al [76] designed and prepared a series of $C_x Hf_{0.25}NbTaW_{0.5}$ composites by vacuum arc melting. The addition of carbon leads to the formation of an FCC carbide phase, which plays an important role. At room temperature, all the composites exhibited high strength and fracture strain (>30%), exceeding those of most of the RHEAs. At high temperatures, the composites also performed well, with YS of 792 MPa at 1473 K and 749 MPa at 1673 K, which also exceeded those of most of the reported RHEAs (Fig. 16 and Fig. 3).

The composites designed by the author exhibited an excellent combination of strength and fracture strain, broadening their potential for industrial application. However, the carbide or nitrides formed in the RHEAs might not have a specific chemical formula, and many of them are multicomponent. SMELTZER et al [104] investigated RHEAs intentionally doped with nonmetallic atoms to form precipitates for obtaining higher hardness. In their work, MoNbTaW doped with N atoms was prepared by liquid nitrogen cryogenic mechanical alloying. It is proven to be successful using this way, as nitride phases were observed in the RHEA. The nitrides formed in the RHEA were in two different forms, identified as ordered laminar tetragonal (Mo,W)(Nb,Ta)N nitride and $(Nb,Ta)_2CN$ complex carbonitride, respectively.

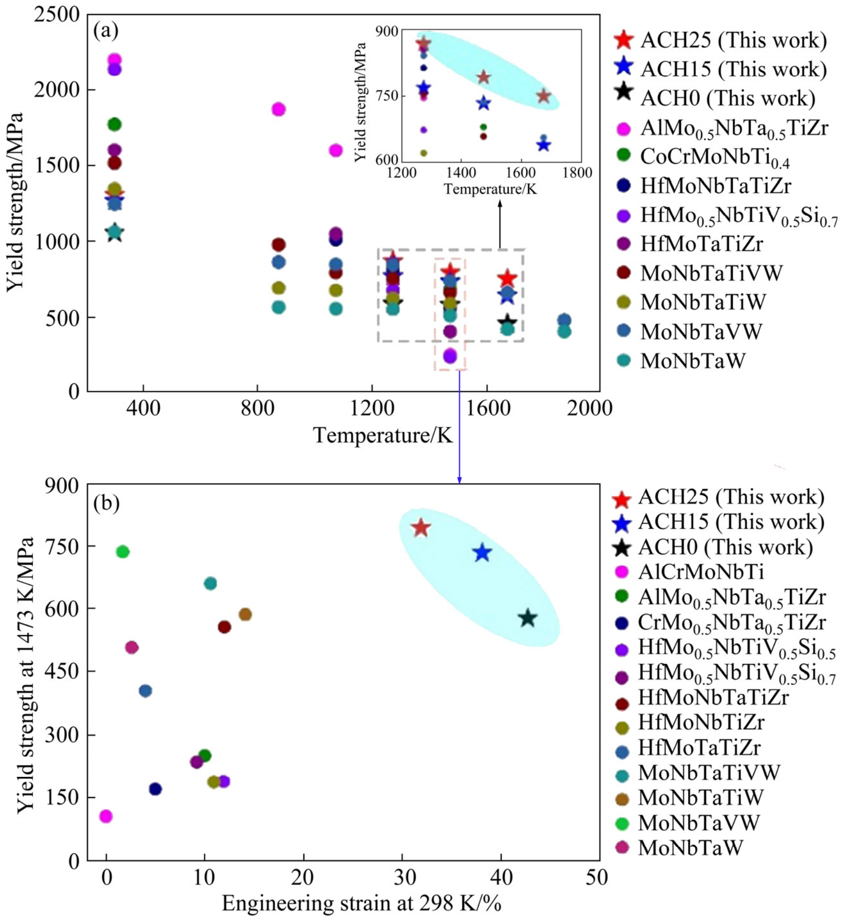

Fig. 16 Temperature dependence of yield strength of C_xHf0.25NbTaW$_{0.5}$ and several classic RHEAs (a), and relationship between yield strength of $C_xHf_{0.25}NbTaW_{0.5}$ and several RHEAs at 1473 K and plasticity at 298 K (b) [19,25,58,74−76,92,93,105−108] (Reproduced under the terms of the Creative Common License)

The complex nitrides formed in the alloy exhibited a cleavage plane deformation mechanism rather than a dislocation-based deformation mechanism common for RHEAs. With the help of the nitrides, the Vickers hardness of the doped RHEA exhibited a peak median hardness up to 17.8 GPa, which was almost 550% that of the cast state. They systematically investigated the N introduction strategy from processing to micro-structure and to mechanical properties. Besides, the precipitating and growing behavior of the nitrides are also figured out by studying the effect of heat treatments. They also demonstrated liquid nitrogen cryogenic mechanical alloying to be an adaptable strategy for the formation of complex nitrides which were only formed under extreme reaction conditions in other ways.

4 Other properties of RHEAs

Recently, RHEAs have attracted more attention because of their mechanical properties and other properties including wear resistance, biocompatibility, oxidation behavior, corrosion, electrical, and irradiation properties.

4.1 Wear resistance

Al is known to be a BCC stabilizing element which has high solubility of Ti, Zr and Hf elements, and is often introduced into HEAs for better tribological properties. However, for RHEAs, many studies were focused on the microstructure and mechanical properties and there only existed a few on tribological properties. BHARDWAJ et al [109] chose TiZrHfNb as a model alloy and introduced Al to enhance the wear resistance by properly designing the alloy composition. Equimolar AlTiZrHfNb consists of a disordered BCC matrix phase and another ordered BCC phase, while other RHEAs with lower Al contents are composed only of the BCC matrix phase. The initial friction coefficient decreased significantly as the hardness increased to HV 420 from HV 229 of the matrix alloy. The introduction of Al significantly improved the wear resistance of the RHEA, which could be attributed to the strengthening of mechanical properties and the formation of oxidative tribolayer. Because no obvious segregation was observed and there existed quite a number of oxides in the wear debris, the key wear mechanism for AlTiZrHfNb was deemed to be oxidative wear.

4.2 Biocompatibility

Owing to their superior biocompatibility and mechanical properties, many RHEAs have been studied as metallic biomaterials, such as Hf−Nb−Ta−Mo−Ti−Zr, Nb−Ta−Mo−Ti−Zr, Hf−Cr−Mo−Ti−Zr, and Nb−Ta−Fe−Ti−Zr systems. However, the alloy designing for biomaterials differs significantly from that of those RHEAs designed for mechanical performance. LIJIMA et al [110] first developed a new Hf−Nb−Ta−Mo−Ti−Zr bioRHEA by combining several alloy designing parameters. They successfully obtained a $Hf_{28.33}Nb_{6.74}Ta_{6.74}Mo_{1.55}Ti_{28.33}Zr_{28.33}$ bioRHEA that had comparable biocompatibility and higher strength compared with the widely used CP-Ti as well as considerable ductility at room temperature. They found that it is effective to use the combined alloy designing strategies in developing non-equiatomic Hf−Nb−Ta−Mo−Ti−Zr bioRHEAs.

Owing to the intrinsic nature of RHEAs, severe segregation is unavoidable. In addition, poor shape flexibility due to limited preparation methods restricts the practical application of bioRHEAs. The newly-developed selective laser melting (SLM) technique has the advantages of customizing shapes and a high cooling rate simultaneously, making it suitable for fabricating bioRHEAs directly; however, pre-alloyed RHEA powders are difficult to obtain owing to their high melting-point. ISHIMOTO et al [111] first developed pre-alloyed $Ti_{1.4}Zr_{1.4}Nb_{0.6}Ta_{0.6}Mo_{0.6}$ powders by modifying the composition of equimolar TiZrNbTaMo to lower the melting point. Similarly, the authors successfully produced bioRHEA parts by SLM that had high density and good compatibility. Moreover, a jungle gym shape without any cracks and deformation or beam fragmentation was also successfully achieved by selective laser melting, as shown in Fig. 17. In terms of mechanical properties, the as-built parts exhibited a yield strength of (1690±78) MPa, which was approximately 48% higher than that of the as-cast parts, which had a YS of 1140 MPa. At the same time, the as-built part broke at a true strain of (1.32±0.19)%, which is moderate by RHEA standards.

The large improvements can be attributed to a combination of grain boundary strengthening (refined grains) and solid-solution strengthening (less elemental segregation and more solid solution) due to the high cooling rate of SLM. As for the biocompatibility, the cell density on the as-built parts was comparable to that on the commonly used CP-Ti and the as-cast parts, and much better than the widely used SS316L parts, indicating good comprehensive compatibility, so the as-built $Ti_{1.4}Zr_{1.4}Nb_{0.6}Ta_{0.6}Mo_{0.6}$ has great potential for future application as a biomaterial. It has been pointed out that single-phase HEAs have better anti-pitting ability than conventional alloys, the good corrosion resistance of TiZrHfNbTa being due mainly to its single BCC phase.

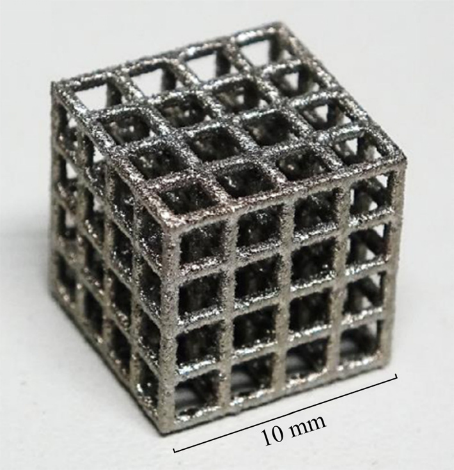

Fig. 17 Appearance of SLM-built jungle gym-shaped product [111] (Reproduced under the terms of the Creative Common License)

4.3 Corrosion properties

LI et al [56] investigated the corrosion mechanism of lightweight $TiCrVNb_{0.5}Al_{0.5}$, as few studies have been focused on their corrosion properties. The lightweight RHEA consists of a single BCC phase without element segregation. The $TiCrVNb_{0.5}Al_{0.5}$ lightweight RHEA has good corrosion resistance, with a low corrosion current density of approximately 10^{-7}–10^{-8} A/cm^2 and a high breakdown potential of 1.8−1.9 V (vs SCE) in 3.5 wt.% NaCl and 1 mol/L HCl solutions. At the same time, it also shows excellent repassivation ability in a chloride environment owing to its single BCC phase composition and passive film containing much Cr^{3+}, Ti^{4+}, and Al^{3+}. Compared with conventional alloys, RHEAs have high atomic-level stresses resulting from the severe lattice distortion which facilitates amorphization after irradiation. After that, local melting and recrystallization happen because of thermal spikes, inducing much fewer defects than traditional alloys. Consequently, RHEAs with good irradiation resistance are promising nuclear materials for application in extreme environments.

4.4 Nuclear applications

RHEAs are potential for advanced nuclear reactor applications due to high melting points and high strengths at elevated temperatures [112,113]. However, their behavior under irradiation damage and complex corrosion environment needs to be investigated further. ZHOU et al [114] investigated phase stability of novel HfNbTaTiVZr under 1 MeV Kr^{2+} ion irradiation at 298 and 423 K. They observed a radiation-induced amorphization at 2 displacements per atom at 298 K and the critical temperature is deduced to be within 298−423 K. The amorphization is facilitated by the system free energy increased by lattice distortion and atomic level strain energy, which lowers the energy difference between crystalline and amorphous state. Similarly, the amorphization was observed by SADEGHILARIDJANI et al [115] in HfTaTiVZr due to lattice distortion and high atomic level strain. Under identical irradiation conditions, HfTaTiVZr shows superior irradiation resistance which has ~20% hardening compared to ~50% hardening for 304 stainless steel. This self-healing ability contributed to the good irradiation resistance, which was related to the sluggish diffusion effect in RHEAs that reduced effective mobility of interstitial and vacancy and limited irradiation induced damage. ZHANG et al [116] designed the novel $Cr_{0.25}Mo_{0.5}NbTiV$ and $Mo_{0.5}NbTiV_{0.5}Zr_{0.25}$, with low thermal neutron absorption cross-section elements for potential accident-tolerant fuel cladding candidate materials. They investigated the short-time corrosion behaviors of the two RHEAs in a simulated pressurized water reactor (PWR) water environment. A double-layer oxide film of Ti, Nb, and V was formed on both the annealed and irradiated RHEAs. Through thorough analysis, the inner oxide grew via an inward diffusion mechanism while the outer oxide particles grew via the dissolution and redeposition process of the metal cations in the vicinity of the water. The authors found that helium ion irradiation offered limited help to both RHEAs on corrosion kinetics because of their intrinsic lattice distortion and sluggish diffusion effects.

4.5 Electronic structure

MU et al [117] used first-principles alloy theory and explored the effect of local lattice distortions of six RHEAs, MoNbTaW, TiZHfNbr, ZrNbVCr, MoNbTaVW, TiZrHfNbTa, and CrNbTiVZr, on the electronic structure, as all the unique properties of RHEAs originate from them. They identified them into two types: one was the small-displacement alloys (MoNbTaW and MoNbVTaW) and relatively the other was the large-displacement alloys (TiZHfNbr, ZrNbVCr, TiZrHfNbTa, and CrNbTiVZr). According to their study, local distortions led to smeared Fermi surfaces of the latter type alloys, resulting in their almost saturated resistivities. Other properties originating from the electronic structure and the relationship between them still need to be studied.

5 Conclusions

The current work reviews recent progress in RHEAs. Because of their attractive performance at high temperatures, much work has been done on RHEAs to find new next-generation high-temperature structural materials. New alloy systems and alloys with new compositions have also been developed. This work helps to identify new potential RHEAs with satisfactory properties. New models and theories have been established and developed, such as the shear lag model and the edge dislocation mechanism. These theoretical results provide help to improve the mechanical properties of RHEAs. Several simulations and calculation techniques have been applied in RHEAs, such as the CALPHAD and *ab initio* methods. The calculated findings save time in the screening of RHEAs that have enormous composition make-ups, providing a better understanding of atomic-level mechanisms.

Many new RHEAs with excellent high-temperature mechanical properties have been developed. Studies have been focused on improving the high-temperature strength and melting points of alloys, and it is now easy to exceed the traditional superalloys that are now commonly used in high-temperature structural applications. Typically, solid-solution strengthening, which leads to high room-temperature strength, weakens at high temperatures. Consequently, researchers have introduced other phases into RHEAs to form eutectics or composites to further improve high-temperature behavior. However, few RHEAs exhibit good ductility at room temperature. The only RHEA with room-temperature tensile ductility is the TiZrHfNbTa system, and no RHEA with better ductility has yet been found. That is to say, they have limited high-temperature strength. Therefore, it is still of vital importance to find a balance between room-temperature ductility and high-temperature strength in RHEAs. Moreover, it is easier to obtain good high-temperature strength than to achieve good room-temperature ductility, making it is much more practical to improve the high-temperature strength of RHEAs which already exhibit good room-temperature ductility. Much work still needs to be done as the introduction of strengthening phases may affect the deformation mechanism. However, achieving a good balance remains difficult.

In addition to their mechanical properties, RHEAs exhibit many other attractive properties. With similar composition to titanium alloys, some Ti−Zr−Nb system RHEAs exhibit good biocompatibility with the preferred mechanical performance. Compared to refractory elements, RHEAs have good irradiation resistance and the potential to be used in nuclear materials. Other properties of RHEAs, such as wear and corrosion resistance, have also been widely studied. There remains a huge space to explore RHEAs in different areas.

Overall, few of the RHEAs that can be applied in practice have been developed until now. However, all RHEAs studied to date exhibit some limitations; therefore, more efforts need to be made for future applications. Based on the existing challenges, research on RHEAs should be focused on the following areas:

(1) Establishing database and collecting more data of RHEAs by shortening the research cycle through additive manufacturing combined with high-throughput experimental method.

(2) Establishing new theories or modifying existing theories, to overcome the trade-off between room-temperature ductility and high-temperature strength.

(3) Making better use of simulations or calculation methods to screen new and promising RHEAs.

(4) Solving the intrinsically poor oxidation resistance at high temperatures through alloy design.

(5) Determining the relationship among atomic-level complexity, microstructure, and macro properties.

Acknowledgments

The anthors are very grateful to the financial supports from the National Natural Science Foundation of China (Nos. 51871147, 51821001), and the Shanghai Aerospace Advanced Technology Joint Research Fund, China (No. USCAST2020-35).

References

[1] GAN Meng-di, CHONG Xiao-yu, JING Feng. Research status and prospects of aerospace high-temperature structural materials [J]. Journal of Kunming University of Science and Technology (Natural Sciences), 2021, 6(46): 24−36. (in Chinese)

[2] HUDA Z, EDI P. Materials selection in design of structures and engines of supersonic aircrafts: A review [J]. Materials & Design, 2013, 46: 552−560.

[3] YEH J W, LIN S J, CHIN T S, GAN J Y, CHEN S K, SHUN T T, TSAU C H, CHOU S Y. Formation of simple crystal structures in Cu−Co−Ni−Cr−Al−Fe−Ti−V alloys with multiprincipal metallic elements [J]. Metallurgical and Materials Transactions A, 2004 35: 2533−2536.

[4] CANTOR B, CHANG I T H, KNIGHT P, VINCENT A J B. Microstructural development in equiatomic multicomponent alloys [J]. Materials Science and Engineering A, 2004, 375/376/377: 213−218.

[5] REN Ming-xing, LI Bang-sheng, FU Heng-zhi. Formation condition of solid solution type high-entropy alloy [J]. Transactions of Nonferrous Metals Society of China, 2013, 23(4): 991−995.

[6] LILENSTEN L, COUZINIÉ J P, BOURGON J, PERRIÈRE L, DIRRAS G, PRIMA F, GUILLOT I. Design and tensile properties of a bcc Ti-rich high-entropy alloy with transformation-induced plasticity [J]. Materials Research Letters, 2017, 5(2): 110−116.

[7] LILENSTEN L, COUZINIÉ J P, PERRIÈRE L, HOCINI A, KELLER C, DIRRAS G, GUILLOT I. Study of a bcc

multi-principal element alloy: Tensile and simple shear properties and underlying deformation mechanisms [J]. Acta Materialia, 2018, 142: 131−141.

[8] HE Zhu-feng, JIA Nan, YAN Hai-le, SHEN Yong-feng, ZHU Ming-wei, GUAN Xian-jun, ZHAO Xiao-li, JIN Shen-bao, SHA Gang, ZHU Yun-tian, LIU C T. Multi-heterostructure and mechanical properties of N-doped FeMnCoCr high entropy alloy [J]. International Journal of Plasticity, 2021, 139: 102965.

[9] SONG Min, ZHOU Rui, GU Ji, WANG Zhang-wei, NI Song, LIU Yong. Nitrogen induced heterogeneous structures overcome strength-ductility trade-off in an additively manufactured high-entropy alloy [J]. Applied Materials Today, 2020, 18: 100498.

[10] HE Feng, WANG Zhi-jun, WU Qing-feng, CHEN Da, YANG Tao, LI Jun-jie, WANG Jin-cheng, LIU C T, KAI Ji-jung. Tuning the defects in face centered cubic high entropy alloy via temperature-dependent stacking fault energy [J]. Scripta Materialia, 2018, 155: 134−138.

[11] LI Bao-yu, PENG Kun, HU Ai-ping, ZHOU Ling-ping, ZHU Jia-jun, LI De-yi. Structure and properties of $FeCoNiCrCu0.5Al_x$ high-entropy alloy [J]. Transactions of Nonferrous Metals Society of China, 2013, 23(3): 735−741.

[12] SHAHMIR H, ASGHARI-RAD P, MEHRANPOUR M S, FORGHANI F, KIM H S, NILI-AHMADABADI M. Evidence of FCC to HCP and BCC-martensitic transformations in a CoCrFeNiMn high-entropy alloy by severe plastic deformation [J]. Materials Science and Engineering A, 2021, 807: 140875.

[13] GAN Guo-yong, MA Li, LUO Dong-ming, JIANG Shan, TANG Bi-yu. Influence of Al substitution for Sc on thermodynamic properties of HCP high entropy alloy $Hf_{0.25}Ti_{0.25}Zr_{0.25}Sc_{0.25-x}Al_x$ from first-principles investigation [J]. Physica B: Condensed Matter, 2020, 593: 412272.

[14] CHEN Jian, ZHOU Xue-yang, WANG Wei-li, LIU Bing, LV Yu-kun, YANG Wei, XU Da-peng, LIU Yong. A review on fundamental of high entropy alloys with promising high−temperature properties [J]. Journal of Alloys and Compounds, 2018, 760: 15−30.

[15] KIM I H, OH H S, LEE K S, PARK E S. Optimization of conflicting properties via engineering compositional complexity in refractory high entropy alloys [J]. Scripta Materialia, 2021, 199: 113839.

[16] TRAVERSIER M, MESTRE-RINN P, PEILLON N, RIGAL E, BOULNAT X, TANCRET F, DHERS J, FRACZKIEWICZ A. Nitrogen-induced hardening in an austenitic CrFeMnNi high-entropy alloy (HEA) [J]. Materials Science and Engineering A, 2021, 804: 140725.

[17] SENKOV O N, GORSSE S, MIRACLE D B. High temperature strength of refractory complex concentrated alloys [J]. Acta Materialia, 2019, 175: 394−405.

[18] SENKOV O N, WILKS G B, MIRACLE D B, CHUANG C P, LIAW P K. Refractory high-entropy alloys [J]. Intermetallics, 2010, 18(9): 1758−1765.

[19] SENKOV O N, WOODWARD C F. Microstructure and properties of a refractory $NbCrMo_{0.5}Ta_{0.5}TiZr$ alloy [J]. Materials Science and Engineering A, 2011, 529: 311−320.

[20] SENKOV O N, SCOTT J M, SENKOVA S V, MIRACLE D B, WOODWARD C F. Microstructure and room temperature properties of a high-entropy TaNbHfZrTi alloy [J]. Journal of Alloys and Compounds, 2011, 509(20): 6043−6048.

[21] SENKOV O N, SCOTT J M, SENKOVA S V., MEISENKOTHEN F, MIRACLE D B, WOODWARD C F. Microstructure and elevated temperature properties of a refractory TaNbHfZrTi alloy [J]. Journal of Materials Science, 2012, 47(9): 4062−4074.

[22] SENKOV O N, SENKOVA S V., MIRACLE D B, WOODWARD C. Mechanical properties of low-density, refractory multi-principal element alloys of the Cr−Nb−Ti−V−Zr system [J]. Materials Science and Engineering A, 2013, 565: 51−62.

[23] SENKOV O N, WOODWARD C, MIRACLE D B. Microstructure and properties of aluminum-containing refractory high-entropy alloys [J]. JOM, 2014, 66(10): 2030−2042.

[24] LEY N A, SEGOVIA S, GORSSE S, YOUNG M L. Characterization and modeling of NbNiTaTiW and NbNiTaTiW−Al refractory high-entropy alloys [J]. Metallurgical and Materials Transactions A, 2019, 50(10): 4867−4876.

[25] LIU Yuan, ZHANG Yan, ZHANG Heng, WANG Nai-juan, CHEN Xiang, ZHANG Hua-wei, LI Yan-xiang. Microstructure and mechanical properties of refractory $HfMo_{0.5}NbTiV_{0.5}Si_x$ high-entropy composites [J]. Journal of Alloys and Compounds, 2017, 694: 869−876.

[26] MING Kai-sheng, BI Xiao-fang, WANG Jian. Realizing strength-ductility combination of coarse-grained $Al_{0.2}Co_{1.5}CrFeNi_{1.5}Ti_{0.3}$ alloy via nano-sized, coherent precipitates [J]. International Journal of Plasticity, 2018, 100: 177−191.

[27] YANG Cheng, AOYAGI K, BIAN Hua-kang, CHIBA A. Microstructure evolution and mechanical property of a precipitation-strengthened refractory high-entropy alloy HfNbTaTiZr [J]. Materials Letters, 2019, 254: 46−49.

[28] DOBBELSTEIN H, GUREVICH E L, GEORGE E P, OSTENDORF A, LAPLANCHE G. Laser metal deposition of compositionally graded TiZrNbTa refractory high-entropy alloys using elemental powder blends [J]. Additive Manufacturing, 2019, 25: 252−262.

[29] YAO H W, QIAO J W, HAWK J A, ZHOU H F, CHEN M W, GAO M C. Mechanical properties of refractory high-entropy alloys: Experiments and modeling [J]. Journal of Alloys and Compounds, 2017, 696: 1139−1150.

[30] XU Qin, CHEN De-zhi, WANG Cong-rui, CAO Wen-chao, WANG Qi, CUI Hong-zhi, ZHANG Shu-yan, CHEN Rui-run. Effects of La on microstructure and mechanical properties of $NbMoTiVSi_{0.2}$ refractory high entropy alloys [J]. Transactions of Nonferrous Metals Society of China, 2021, 31(2): 512−520.

[31] CHEN Qiu-shi, LU Yi-ping, DONG-yong, WANG Tong-min, LI Ting-ju. Effect of minor B addition on microstructure and properties of AlCoCrFeNi multi-compenent alloy [J]. Transactions of Nonferrous Metals Society of China, 2015, 25(9): 2958−2964.

[32] MU Yong-kun, LIU Hong-xi, LIU Ya-hui, ZHANG Xiao-wei, JIANG Ye-hua, DONG Tao. An *ab initio* and experimental studies of the structure, mechanical parameters and state density on the refractory high-entropy alloy systems [J].

Journal of Alloys and Compounds, 2017, 714: 668−680.

[33] MCALPINE S W, LOGAN J V., SHORT M P. Predicting single phase stability and segregation in the NbMoTaTi–(W,V) high entropy alloy system with the vacancy exchange potential [J]. Scripta Materialia, 2021, 191: 29−33.

[34] SENKOV O N, ZHANG C, PILCHAK A L, PAYTON E J, WOODWARD C, ZHANG F. CALPHAD-aided development of quaternary multi-principal element refractory alloys based on NbTiZr [J]. Journal of Alloys and Compounds, 2019, 783: 729−742.

[35] SHAIKH S M, HARIHARAN V S, YADAV S K, MURTY B S. CALPHAD and rule-of-mixtures: A comparative study for refractory high entropy alloys [J]. Intermetallics, 2020, 127: 106926.

[36] LIANG Xiu-bing, WAN Yi-xing, MO Jin-yong, HU Zhen-feng, CHEN Yong-xiong. Research progress in novel high-temperature high entropy alloys [J]. Science & Technology Review, 2021, 39(11): 96−108. (in Chinese)

[37] LIU Zhang-quan, QIAO Jun-wei. Research progress of refractory high-entropy alloys [J]. Materials China, 2019, 38(8): 768−774. (in Chinese)

[38] WEI Yao-guang, GUO Gang, LI Jing, ZENG Yi-pan, JING He. Application of refractory high entropy alloys on aero-engines [J]. Journal of Aeronautical Materials, 2019, 39(5): 82−93. (in Chinese)

[39] LI Yan-chao, LI Lai-ping, GAO Xuan-qiao, ZHANG Wen, LIN Xiao-hui, XUE Jian-rong, ZHANG Guo-jun. Research progress on refractory high entropy alloys [J]. Rare Metal Materials and Engineering, 2020, 49(12): 4365−4372. (in Chinese)

[40] GAO Niu, LIU Xin-wang, WU Wei-feng, BAI Zhu-cheng, YAO Jun-qing, FAN Zi-tian. Advances of the strengthening and toughening of high-entropy multi-principal-element heat-resistant alloys [J]. Materials Reports, 2021, 35(17): 17037−17042. (in Chinese)

[41] CAO Yuan-kui, LIU Yong, LIU Bin, ZHANG Wei-dong, WANG Jia-wen, DU Meng. Effects of Al and Mo on high temperature oxidation behavior of refractory high entropy alloys [J]. Transactions of Nonferrous Metals Society of China, 2019, 29(7): 1476−1483.

[42] WU Yi-dong, WANG Qin-jia, LIN De-ye, CHEN Xiao-hua, WANG Tan, WANG W Y, WANG Yan-dong, HUI Xi-dong. Phase stability and deformation behavior of TiZrHfNbO high-entropy alloys [J]. Frontiers in Materials, 2020, 7: 589052.

[43] YASUDA H Y, YAMADA Y, CHO Ken, NAGASE T. Deformation behavior of HfNbTaTiZr high entropy alloy singe crystals and polycrystals [J]. Materials Science and Engineering A, 2021, 809: 140983.

[44] GEORGE E P, CURTIN W A, TASAN C C. High entropy alloys: A focused review of mechanical properties and deformation mechanisms [J]. Acta Materialia, 2020, 188: 435−474.

[45] WEN Xiao-can, WU Yuan, HUANG Hai-long, JIANG Sui-he, WANG Hui, LIU Xiong-jun, ZHANG Yong, WANG Xian-zhen, LU Zhao-ping. Effects of Nb on deformation-induced transformation and mechanical properties of HfNb$_x$Ta$_{0.2}$TiZr high entropy alloys [J]. Materials Science and Engineering A, 2021, 805: 140798.

[46] ZHANG Y, ZHOU Y J, LIN J P, CHEN G L, LIAW P K. Solid-solution phase formation rules for multi-component alloys [J]. Advanced Engineering Materials, 2008, 10(6): 534−538.

[47] YANG X, ZHANG Y. Prediction of high-entropy stabilized solid-solution in multi-component alloys [J]. Materials Chemistry and Physics, 2012, 132(2/3): 233−238.

[48] GUO Sheng, NG Chun, LU Jian, LIU C T. Effect of valence electron concentration on stability of fcc or bcc phase in high entropy alloys [J]. Journal of Applied Physics, 2011, 109(10): 103505.

[49] SHEIKH S, SHAFEIE S, HU Q, AHLSTRÖM J, PERSSON C, VESELÝ J, ZÝKA J, KLEMENT U, GUO S. Alloy design for intrinsically ductile refractory high-entropy alloys [J]. Journal of Applied Physics, 2016, 120(16): 164902.

[50] SENKOV O N, SENKOVA S V., WOODWARD C, MIRACLE D B. Low-density, refractory multi-principal element alloys of the Cr−Nb−Ti−V−Zr system: Microstructure and phase analysis [J]. Acta Materialia, 2013, 61(5): 1545−1557.

[51] SENKOV O N, SENKOVA S V, WOODWARD C. Effect of aluminum on the microstructure and properties of two refractory high-entropy alloys [J]. Acta Materialia, 2014, 68: 214−228.

[52] SENKOV O N, JENSEN J K, PILCHAK A L, MIRACLE D B, FRASER H L. Compositional variation effects on the microstructure and properties of a refractory high-entropy superalloy AlMo0.5NbTa0.5TiZr [J]. Materials & Design, 2018, 139: 498−511.

[53] SENKOV O N, RAO S, CHAPUT K J, WOODWARD C. Compositional effect on microstructure and properties of NbTiZr-based complex concentrated alloys [J]. Acta Materialia, 2018, 151: 201−215.

[54] NONG Zhi-sheng, ZHU Jing-chuan, YU Hai-ling, LAI Zhong-hong. First principles calculation of intermetallic compounds in FeTiCoNiVCrMnCuAl system high entropy alloy [J]. Transactions of Nonferrous Metals Society of China, 2012, 22(6): 1437−1444.

[55] PAN Jia-yi, DAI Ting, LU Tao, NI Xu-yao, DAI Jian-wen, LI Miao. Microstructure and mechanical properties of Nb25Mo25Ta25W25 and Ti8Nb23Mo23Ta23W23 high entropy alloys prepared by mechanical alloying and spark plasma sintering [J]. Materials Science and Engineering A, 2018, 738: 362−366.

[56] LI Meng-jiao, CHEN Qing-jun, CUI Xia, PENG Xin-yuan, HUANG Guo-sheng. Evaluation of corrosion resistance of the single-phase light refractory high entropy alloy TiCrVNb0.5Al0.5 in chloride environment [J]. Journal of Alloys and Compounds, 2021, 857: 158278.

[57] YURCHENKO N, PANINA E, TIKHONOVSKY M, SALISHCHEV G, ZHEREBTSOV S, STEPANOV N. Structure and mechanical properties of an in situ refractory Al$_{20}$Cr$_{10}$Nb$_{15}$Ti$_{20}$V$_{25}$Zr$_{10}$ high entropy alloy composite [J]. Materials Letters, 2020, 264: 127372.

[58] GUO N N, WANG L, LUO L S, LI X Z, SU Y Q, GUO J J, FU H Z. Microstructure and mechanical properties of refractory MoNbHfZrTi high-entropy alloy [J]. Materials & Design, 2015, 81: 87−94.

[59] CHENG Peng, ZHAO Yu-hong, XU Xiao-tao, WANG Shuai,

SUN Yuan-yang, HOU Hua. Microstructural evolution and mechanical properties of $Al_{0.3}CoCrFeNiSi_x$ high-entropy alloys containing coherent nanometer-scaled precipitates [J]. Materials Science and Engineering A, 2020, 772: 138681.

[60] SENKOV O N, COUZINIE J P, RAO S I, SONI V, BANERJEE R. Temperature dependent deformation behavior and strengthening mechanisms in a low density refractory high entropy alloy $Al_{10}Nb_{15}Ta_5Ti_{30}Zr_{40}$ [J]. Materialia, 2020, 9: 100627.

[61] SONI V, SENKOV O N, COUZINIE J P, ZHENG Y, GWALANI B, BANERJEE R. Phase stability and microstructure evolution in a ductile refractory high entropy alloy $Al_{10}Nb_{15}Ta_5Ti_{30}Zr_{40}$ [J]. Materialia, 2020, 9: 100569.

[62] KANG B, LEE J, RYU H J, HONG S H. Ultra-high strength WNbMoTaV high-entropy alloys with fine grain structure fabricated by powder metallurgical process [J]. Materials Science and Engineering A, 2018, 712: 616−624.

[63] GUO Wen-min, LIU Bin, LIU Yong, LI Tian-chen, FU Ao, FANG Qi-hong, NIE Yan. Microstructures and mechanical properties of ductile NbTaTiV refractory high entropy alloy prepared by powder metallurgy [J]. Journal of Alloys and Compounds, 2019, 776: 428−436.

[64] KANG B, LEE Jun-ho, RYU H J, HONG S H. Microstructure, mechanical property and Hall−Petch relationship of a light-weight refractory $Al_{0.1}CrNbVMo$ high entropy alloy fabricated by powder metallurgical process [J]. Journal of Alloys and Compounds, 2018, 767: 1012−1021.

[65] LIU Bin, WANG Jing-shi, CHEN Jian, FANG Qi-hong, LIU Yong. Ultra-high strength TiC/refractory high-entropy-alloy composite prepared by powder metallurgy [J]. JOM, 2017, 69(4): 651−656.

[66] LIU Yong, CAO Yuan-kui, WU Wen-qian, SONG Min, ZHANG Wei, LIU Bin. Progress of powder metallurgical high entropy alloys [J]. The Chinese Journal of Nonferrous Metals, 2019, 29(9): 2155−2184. (in Chinese)

[67] ROH A, KIM D, NAM S, KIM D I, KIM H Y, LEE K A, CHOI H, KIM J H. NbMoTaW refractory high entropy alloy composites strengthened by in-situ metal-non-metal compounds [J]. Journal of Alloys and Compounds, 2020, 822: 153423.

[68] LV Sha-sha, ZU Yu-fei, CHEN Guo-qing, ZHAO Bo-jun, FU Xue-song, ZHOU Wen-long. A multiple nonmetallic atoms co-doped CrMoNbWTi refractory high-entropy alloy with ultra-high strength and hardness [J]. Materials Science and Engineering A, 2020, 795: 140035.

[69] DOBBELSTEIN H, THIELE M, GUREVICH E L, GEORGE E P, OSTENDORF A. Direct metal deposition of refractory high entropy alloy MoNbTaW [J]. Physics Procedia, 2016, 83: 624−633.

[70] DOBBELSTEIN H, GUREVICH E L, GEORGE E P, OSTENDORF A, LAPLANCHE G. Laser metal deposition of a refractory TiZrNbHfTa high-entropy alloy [J]. Additive Manufacturing, 2018, 24: 386−390.

[71] LIU Qi, WANG Yu-dai, ZHENG Hang, TANG Kang, DING Li, LI Huai-xue, GONG Shui-li. Microstructure and mechanical properties of LMD−SLM hybrid forming Ti6Al4V alloy [J]. Materials Science and Engineering A, 2016, 660: 24−33.

[72] ZHANG Hang, XU Wang, XU Yun-jing, LU Zhong-liang, LI Di-chen. The thermal-mechanical behavior of WTaMoNb high-entropy alloy via selective laser melting (SLM): experiment and simulation [J]. The International Journal of Advanced Manufacturing Technology, 2018, 96(1/2/3/4): 461−474.

[73] SENKOV O N, WILKS G B, SCOTT J M, MIRACLE D B. Mechanical properties of $Nb_{25}Mo_{25}Ta_{25}W_{25}$ and $V_{20}Nb_{20}Mo_{20}Ta_{20}W_{20}$ refractory high entropy alloys [J]. Intermetallics, 2011, 19(5): 698−706.

[74] JUAN C C, TSAI M H, TSAI C W, LIN C M, WANG W R, YANG C C, CHEN S K, LIN S J, YEH J W. Enhanced mechanical properties of HfMoTaTiZr and HfMoNbTaTiZr refractory high-entropy alloys [J]. Intermetallics, 2015, 62: 76−83.

[75] WANG Qing, HAN Jin-can, LIU Yu-feng, ZHANG Zhong-wei, DONG Chuang, LIAW P K. Coherent precipitation and stability of cuboidal nanoparticles in body-centered-cubic $Al_{0.4}Nb_{0.5}Ta_{0.5}TiZr_{0.8}$ refractory high entropy alloy [J]. Scripta Materialia, 2021, 190: 40−45.

[76] WU Shi-yu, QIAO Dong-xu, ZHANG Hai-tao, MIAO Jun-wei, ZHAO Hong-liang, WANG Jun, LU Yi-ping, WANG Tong-min, LI Ting-ju. Microstructure and mechanical properties of $C_xHf_{0.25}NbTaW_{0.5}$ refractory high-entropy alloys at room and high temperatures [J]. Journal of Materials Science & Technology, 2022, 97: 229−238.

[77] WANG M, MA Z L, XU Z Q, CHENG X W. Designing $V_xNbMoTa$ refractory high-entropy alloys with improved properties for high-temperature applications [J]. Scripta Materialia, 2021, 191: 131−136.

[78] WEI Qin-qin, SHEN Qiang, ZHANG Jian, CHEN Ben, LUO Guo-qiang, ZHANG Lian-meng. Microstructure and mechanical property of a novel ReMoTaW high-entropy alloy with high density [J]. International Journal of Refractory Metals and Hard Materials, 2018, 77(May): 8−11.

[79] WEI Qin-qin, SHEN Qiang, ZHANG Jian, ZHANG Yin, LUO Guo-qiang, ZHANG Lian-meng. Microstructure evolution, mechanical properties and strengthening mechanism of refractory high-entropy alloy matrix composites with addition of TaC [J]. Journal of Alloys and Compounds, 2019, 777: 1168−1175.

[80] WEI Qin-qin, LUO Guo-qiang, TU Rong, ZHANG Jian, SHEN Qiang, CUI Yu-jie, GUI Yun-wei, CHIBA A. High-temperature ultra-strength of dual-phase $Re_{0.5}MoNbW\text{-}(TaC)_{0.5}$ high-entropy alloy matrix composite [J]. Journal of Materials Science & Technology, 2021, 84: 1−9.

[81] WEI Q Q, XU X D, LI G M, LUO G Q, ZHANG J, SHEN Q, WU C L. A carbide-reinforced $Re_{0.5}MoNbW(TaC)_{0.8}$ eutectic high-entropy composite with outstanding compressive properties [J]. Scripta Materialia, 2021, 200: 113909.

[82] WEI Qin-qin, LUO Guo-qiang, ZHANG Jian, JIANG Shi-jing, CHEN Ping-an, SHEN Qiang, ZHANG L M. Designing high entropy alloy-ceramic eutectic composites of $MoNbRe_{0.5}TaW(TiC)_x$ with high compressive strength [J]. Journal of Alloys and Compounds, 2020, 818: 152846.

[83] SUZUKI H. A theory of solid solution hardening in body-centred cubic alloys [M]. Vandenhoeck & Ruprecht, 1971.

[84] MARESCA F, CURTIN W A. Theory of screw dislocation strengthening in random BCC alloys from dilute to

"High-Entropy" alloys [J]. Acta Materialia, 2020, 182: 144−162.

[85] MARESCA F, CURTIN W A. Mechanistic origin of high strength in refractory BCC high entropy alloys up to 1900 K [J]. Acta Materialia, 2020, 182: 235−249.

[86] LEE C, MARESCA F, FENG Rui, CHOU Yi, UNGAR T, WIDOM M, AN Ke, POPLAWSKY J D, CHOU Y C, LIAW P K, CURTIN W A. Strength can be controlled by edge dislocations in refractory high-entropy alloys [J]. Nature Communications, 2021, 12: 5474.

[87] SENKOV O N, SENKOVA S V, DIMIDUK D M, WOODWARD C, MIRACLE D B. Oxidation behavior of a refractory $NbCrMo_{0.5}Ta_{0.5}TiZr$ alloy [J]. Journal of Materials Science, 2012, 47(18): 6522−6534.

[88] COUZINIÉ J P, LILENSTEN L, CHAMPION Y, DIRRAS G, PERRIÈRE L, GUILLOT I. On the room temperature deformation mechanisms of a TiZrHfNbTa refractory high-entropy alloy [J]. Materials Science and Engineering A, 2015, 645: 255−263.

[89] ELETI R R, BHATTACHARJEE T, SHIBATA A, TSUJI N. Unique deformation behavior and microstructure evolution in high temperature processing of HfNbTaTiZr refractory high entropy alloy [J]. Acta Materialia, 2019, 171: 132−145.

[90] CHEN Shu-ying, LI Wei-dong, MENG Fan-chao, TONG Yang, ZHANG Hua, TSENG Ko Kai, YEH J W, REN Yang, XU Fei, WU Zheng-gang, LIAW P K. On temperature and strain-rate dependence of flow serration in HfNbTaTiZr high-entropy alloy [J]. Scripta Materialia, 2021, 200: 113919.

[91] LEI Zhi-feng, LIU Xiong-jun, WU Yuan, WANG Hui, JIANG Sui-he, WANG Shu-dao, HUI Xi-dong, WU Yi-dong, GAULT B, KONTIS P, RAABE D, GU Lin, ZHANG Qing-hua, CHEN Hou-wen, WANG Hong-tao, LIU Jia-bin, AN Ke, ZENG Qiao-shi, NIEH T G, LU Z P. Enhanced strength and ductility in a high-entropy alloy via ordered oxygen complexes [J]. Nature, 2018, 563(7732): 546−550.

[92] HAN Z D, LUAN H W, LIU X, CHEN N, LI X Y, SHAO Y, YAO K F. Microstructures and mechanical properties of $Ti_xNbMoTaW$ refractory high-entropy alloys [J]. Materials Science and Engineering A, 2018, 712: 380−385.

[93] HAN Z D, CHEN N, ZHAO S F, FAN L W, YANG G N, SHAO Y, YAO K F. Effect of Ti additions on mechanical properties of NbMoTaW and VNbMoTaW refractory high entropy alloys [J]. Intermetallics, 2017, 84: 153−157.

[94] TODA-CARABALLO I, RIVERA-DÍAZ-DEL-CASTILLO P E J. Modelling solid solution hardening in high entropy alloys [J]. Acta Materialia, 2015, 85: 14−23.

[95] SENKOV O N, ISHEIM D, SEIDMAN D N, PILCHAK A L. Development of a refractory high entropy superalloy [J]. Entropy, 2016, 18(3): 102.

[96] GUO N N, WANG L, LUO L S, LI X Z, CHEN R R, SU Y Q, GUO J J, FU H Z. Microstructure and mechanical properties of in-situ MC-carbide particulates-reinforced refractory high-entropy $Mo_{0.5}NbHf_{0.5}ZrTi$ matrix alloy composite [J]. Intermetallics, 2016, 69: 74−77.

[97] GUO N N, WANG L, LUO L S, LI X Z, CHEN R R, SU Y Q, GUO J J, FU H Z. Microstructure and mechanical properties of refractory high entropy $(Mo_{0.5}NbHf_{0.5}ZrTi)BCC/M5Si3$ in-situ compound [J]. Journal of Alloys and Compounds, 2016, 660: 197−203.

[98] SOSA J M, JENSEN J K, HUBER D E, VISWANATHAN G B, GIBSON M A, FRASER H L. Three-dimensional characterisation of the microstructure of an high entropy alloy using STEM/HAADF tomography [J]. Materials Science and Technology, 2015, 31(10): 1250−1258.

[99] MA Yue, HAO Jia-miao, JIE Jin-chuan, WANG Qing, DONG Chuang. Coherent precipitation and strengthening in a dual-phase $AlNi_2Co_2Fe_{1.5}Cr_{1.5}$ high-entropy alloy [J]. Materials Science and Engineering A, 2019, 764: 138241.

[100] WANG Rui, ZHU Guo-liang, YANG Chao, WANG Wei, WANG Dong-hong, DONG An-ping, SHU Da, ZHANG Liang, SUN Bao-de. Nano-size carbide-reinforced Ni matrix composite prepared by selective laser melting [J]. Nano Materials Science, 2019, 2(4): 316−322.

[101] PARK J G, KEUM D H, LEE Y H. Strengthening mechanisms in carbon nanotube-reinforced aluminum composites [J]. Carbon, 2015, 95: 690−698.

[102] HE J Y, WANG H, HUANG H L, XU X D, CHEN M W, WU Y, LIU X J, NIEH T G, AN K, LU Z P. A precipitation-hardened high-entropy alloy with outstanding tensile properties [J]. Acta Materialia, 2016, 102: 187−196.

[103] WANG Rui, WANG Wei, ZHU Guo-liang, PAN Wei-tao, ZHOU Wen-zhe, WANG Dong-hong, LI Fei, HUANG Hai-jun, JIA Yi-wang, DU Da-fan, DONG An-ping, SHU Da, SUN Bao-de. Microstructure and mechanical properties of the TiN particles reinforced IN718C composite [J]. Journal of Alloys and Compounds, 2018, 762: 237−245.

[104] SMELTZER J A, HORNBUCKLE B C, GIRI A K, DARLING K A, HARMER M P, CHAN H M, MARVEL C J. Nitrogen-induced hardening of refractory high entropy alloys containing laminar ordered phases [J]. Acta Materialia, 2021, 211: 116884.

[105] WU Shao-jie, WANG Xiao-di, LU Jin-tao, QU Rui-tao, ZHANG Zhe-feng. Room-temperature mechanical properties of $V_{20}Nb_{20}Mo_{20}Ta_{20}W_{20}$ high-entropy alloy [J]. Advanced Engineering Materials, 2018, 20(7): 1800028.

[106] ZHANG Mi-na, ZHOU Xiang-lin, ZHU Wu-zhi, LI Jing-hao. Influence of annealing on microstructure and mechanical properties of refractory $CoCrMoNbTi_{0.4}$ high-entropy alloy [J]. Metallurgical and Materials Transactions A, 2018, 49(4): 1313−1327.

[107] JENSEN J K, WELK B A, WILLIAMS R E A, SOSA J M, HUBER D E, SENKOV O N, VISWANATHAN G B, FRASER H L. Characterization of the microstructure of the compositionally complex alloy $Al_1Mo_{0.5}Nb_1Ta_{0.5}Ti_1Zr_1$ [J]. Scripta Materialia, 2016, 121: 1−4.

[108] CHEN H, KAUFFMANN A, GORR B, SCHLIEPHAKE D, SEEMÜLLER C, WAGNER J N, CHRIST H J, HEILMAIER M. Microstructure and mechanical properties at elevated temperatures of a new Al-containing refractory high-entropy alloy Nb−Mo−Cr−Ti−Al [J]. Journal of Alloys and Compounds, 2016, 661: 206−215.

[109] BHARDWAJ V, ZHOU Qing, ZHANG Fan, HAN Wei-chao, DU Yin, HUA Ke, WANG Hai-feng. Effect of Al addition on the microstructure, mechanical and wear properties of TiZrNbHf refractory high entropy alloys [J]. Tribology International, 2021, 160: 107031.

[110] IIJIMA Y, NAGASE T, MATSUGAKI A, WANG P, AMEYAMA K, NAKANO T. Design and development of Ti−Zr−Hf−Nb−Ta−Mo high-entropy alloys for metallic biomaterials [J]. Materials & Design, 2021, 202: 109548.

[111] ISHIMOTO T, OZASA R, NAKANO K, WEINMANN M, SCHNITTER C, STENZEL M, MATSUGAKI A, NAGASE T, MATSUZAKA T, TODAI M, KIM H S, NAKANO T. Development of TiNbTaZrMo bio-high entropy alloy (BioHEA) super-solid solution by selective laser melting, and its improved mechanical property and biocompatibility [J]. Scripta Materialia, 2021, 194: 113658.

[112] WANG Xue-jiao, QIAO Jun-wei, WU Yu-cheng. High entropy alloys: The new irradiation-resistant candidate materials towards the fusion reactors [J]. Materials Reports, 2020, 34(9): 17058−17066.

[113] LI Tian-xin, LU Yi-ping, CAO Zhi-qiang, WANG Tong-min, LI Ting-ju. Opportunity and challenge of refractory high-entropy alloys in the field of reactor structural materials [J]. Acta Metallurgica Sinica, 2021, 57(1): 42−54.

[114] ZHOU Jian-ren, KIRK M, BALDO P, GUO Sheng-min, LU Feng-yuan. Phase stability of novel HfNbTaTiVZr refractory high entropy alloy under ion irradiation [J]. Materials Letters, 2021, 305: 130789.

[115] SADEGHILARIDJANI M, AYYAGARI A, MUSKERI S, HASANNAEIMI V, SALLOOM R, CHEN Wei-ying, MUKHERJEE S. Ion irradiation response and mechanical behavior of reduced activity high entropy alloy [J]. Journal of Nuclear Materials, 2020, 529: 151955.

[116] ZHANG Zi-jian, HAN En-hou, XIANG Chao. Effect of helium ion irradiation on short-time corrosion behavior of two novel high-entropy alloys in simulated PWR primary water [J]. Corrosion Science, 2021, 191: 109742.

[117] MU S, WIMMER S, MANKOVSKY S, EBERT H, STOCKS G M. Influence of local lattice distortions on electrical transport of refractory high entropy alloys [J]. Scripta Materialia, 2019, 170: 189−194.

难熔高熵合金综述

田雨生，周文哲，谭庆彪，吴明旭，乔 绅，祝国梁，董安平，疏 达，孙宝德

上海交通大学 材料科学与工程学院 上海市先进高温材料及其精密成形重点实验室和
金属基复合材料国家重点实验室，上海 200240

摘 要：综述了近年来难熔高熵合金(RHEAs)在合金设计、显微组织和力学性能方面的研究进展，并重点讨论了内在的强化机制和变形行为。难熔高熵合金主要由近等摩尔比的难熔元素组成，具有优异的力学性能，尤其是高温力学性能。然而，大多数难熔高熵合金的室温塑性有限。为了解决这一问题，研究人员已开展了大量相关研究工作，其中某些难熔高熵合金材料具有很大的高温实际应用潜力。难熔高熵合金除了具有优异的力学性能外，在其他性能方面也有优势，如生物相容性和耐磨性。最后，还讨论了难熔高熵合金目前存在的问题和对未来发展的建议。

关键词：难熔高熵合金；显微组织；高温强度；力学性能；位错

(Edited by Bing YANG)